VOLUME 5 ISSUE 3 OCTOBER 2020

IJEG

International Journal of Engineering and Geosciences

e-ISSN 2548-0960

The International Journal of Engineering and Geosciences (IJEG)

The International Journal of Engineering and Geosciences (IJEG) is a tri-annually published journal. The journal includes a wide scope of information on scientific and technical advances in the geomatics sciences. The International Journal of Engineering and Geosciences aims to publish pure and applied research in geomatics engineering and technologies. IJEG is a double peer-reviewed (blind) OPEN ACCESS JOURNAL that publishes professional level research articles and subject reviews exclusively in English. It allows authors to submit articles online and track his or her progress via its web interface. All manuscripts will undergo a refereeing process; acceptance for publication is based on at least two positive reviews. The journal publishes research and review papers, professional communication, and technical notes. IJEG does not charge for any article submissions or for processing.

CORRESPONDENCE ADDRESS
Journal Contact: engineeringandgeoscience@gmail.com

CONTENTS

Volume 5 - Issue 3

ARTICLES

International Journal of Engineering and Geosciences (IJEG),
Vol; 5, Issue; 3, pp. 120-129, October, 2020, ISSN 2548-0960, Turkey,
DOI: 10.26833/ijeg.638669

OPPORTUNITIES PROVIDED BY REMOTE SENSING DATA FOR WATERSHED MANAGEMENT: EXAMPLE OF KONYA CLOSED BASIN

Nur Yagmur [1*], Aysegul Tanik [2], Aylin Tuzcu [1], Nebiye Musaoglu [1], Esra Erten [1], Baha Bilgilioglu [3]

[1] ITU, Civil Engineering Faculty, Dept. of Geomatics Engineering, Istanbul, Turkey (yagmurn/tuzcuay/musaoglune/eerten@itu.edu.tr); **ORCID 0000-0002-5915-6929, ORCID 0000-0003-2786-2033, ORCID 0000-0002-8022-8755, ORCID 0000-0002-4208-7170,**
[2] ITU, Civil Engineering Faculty, Dept. of Environmental Engineering, Istanbul, Turkey (tanika@itu.edu.tr); **ORCID 0000-0002-0319-0298**
[3] Gumushane University, Dept. of Geomatics Engineering, Gumushane, Turkey (bbilgilioglu@gumushane.edu.tr); **ORCID 0000-0001-6950-4336**

*Corresponding Author, Received: 26/10/2019, Accepted: 17/02/2020

ABSTRACT: Remote sensing data provides great opportunities in various steps of watershed management like characterization of watersheds that bear dynamic structure with large land, monitoring the physical variations within the basin, and conducting various scenario analyses to detect the response of the basin. The high resolution capacity of today's satellite images enables the production of land use/cover data of a basin in shorter period of time. In this study, it is aimed to demonstrate various aspects of remote sensing technology to be used in watershed management studies. For that purpose, MODIS, Landsat and Sentinel satellite data with different spatial resolutions were used to monitor the surface water bodies in Konya Closed Basin (KCB) of Turkey. In addition, high spatial Worldview-3 satellite data were used to extract detailed information about Akgol Wetland located in KCB. A methodology was developed on the utilization of remote sensing technology consisting of 3 main groups; field surveys, satellite images and ancillary data. In the study, 5 different spectral indices were applied to Sentinel 2 data to determine the areas of surface water bodies. Moreover, Support Vector Machine (SVM) method was applied to Worldview-3 satellite image to classify Akgol Wetland and its vicinity. The importance of establishing watershed information system together with a database reflecting the characteristics of watersheds was underlined. Various examples were given from KCB that is known as the largest closed basin of the country with a surface area of 5.426.480 ha. The basin owns 17 water bodies out of which 2 of them are RAMSAR sites. Within the scope of the study, information obtained from optical and synthetic aperture radar (SAR) satellite images in the basin were discussed. More accurate results were achieved by Sentinel 2 than MODIS and Landsat data. In addition, detailed information about the wetland were extracted by means of Worldview-3 data and water bodies were monitored in all weather conditions via Sentinel 1 SAR data.

Keywords: *Konya Closed Basin, MODIS, Sentinel, Landsat, Worldview- 3*

International Journal of Engineering and Geosciences (IJEG),
Vol; 5, Issue; 3, pp. 120-129, October, 2020,

1. INTRODUCTION

Integrated watershed management has been internationally recognized as an important holistic approach towards natural resources management within the context of sustainable development. Countries have already accepted this understanding and great achievements have recently been realized in regard to conserving water, land and vegetation. The success of various management strategies developed so far depends on the establishment of a good/satisfactory database named as 'watershed information system' (Tanik, 2019). If the database formed stores the minimum data required to define the prevailing characteristics of the watershed of concern, it may further be utilized for various watershed analyses, terrain and/or water quality modelling, and for management of the overall basin (Randhir, 2007; EPA, 2008). Resource inventory required to characterize the watersheds covers the collection, analysis and presentation of data including the following components (UN, 1997);

- Topography and landform
- Geology and geomorphology
- Soils
- Climate
- Hydrology
- Ecology.

At this stage, Remote Sensing (RS) technology enables to generate spatial and temporal data of a number of physical attributes about the watershed surface that can be utilized to map the extent of land and water bodies at watershed scale, and to monitor their dynamics at regular and frequent time intervals (Huang et al., 2018). With the development of RS technology, it has become possible to achieve high resolution data. In order to extract information from satellite image data, different image processing techniques such as spectral indexes, pixel based and object-based classification can be used. Li et al. (2015) compared the performance of various MODIS derived indices to monitor spatio-temporal dynamics of hydrology in seasonally-flooded wetlands. Ludwig et al. (2019) identified suitable spectral indices sensitive to water and wetness using feature selection methods based on mutual information between optical indices and occurrence of water and wetness. Lamb et al. (2019) used spectral indexes and classification methods to determine the spatial extent and vegetation characteristics of tidal wetlands and their change by using Sentinel-1A, Phased Array type L-band Synthetic Aperture Radar (PALSAR), PALSAR-2, Sentinel-2A, and Landsat 8 imagery. Additionally, these methods can be utilized for different purposes such as mapping burned forest areas (Comert et al. 2019), classification of land use/land cover (Heumann, 2011). Comert et al. (2019) detected burned forest areas in Kumluca and Adrasan in Antalya, Turkey with 99% overall accuracy via using Landsat 8 data. Karakus et al. (2017) compared pixel-based and object-based classification techniques by using SPOT 5 data and similar results were obtained.

The objective of this study was to demonstrate the opportunities provided by RS data to be further applied in watershed management. Examples of data produced and/or processed by RS technology were given for Konya Closed Basin (KCB) of Turkey. It is important to note here that available and produced data were stored in the database of the watershed that formed the integral part of 'Watershed Information System'. Every basin has to bear an information system of its own, as each watershed has its intrinsic properties not similar to even the neighborhood basin.

2. STUDY AREA

KCB located at the Central Anatolia in Turkey has been declared as one of the 200 significant ecologically important regions of the world by the World Wildlife Foundation (WWF) (Dursun et al., 2012). It is located between 36° 51' N and 39° 29'N latitudes, 31° 36'E and 34° 52'E longitudes. It covers almost 7% of Turkey's overall surface area and bears an annual amount of 4,365 billion m^3 of usable water. However, water consumption of 6,5 billion m^3 in the basin points out that there is an annual water deficit of approximately 2 billion m^3. Thus, this basin is known to be one of the significant basins of the country facing water scarcity problem. Semi-arid climatic conditions prevail in the basin. The average annual rainfall was around 407 mm taking into account the average of all years from 1923 to 2013. However, this annual precipitation value was found lower in this study that considered the 1984-2017 period. Larger surface areas of non-flowing water bodies with lower precipitation and higher evaporation are the significant characteristics of the basin compared to country's average meteorological status; however, the basin exerts an interesting water balance (CCIWR, 2016). It consists of only 2% of the country's overall surface water resources whereas involves 17% of the groundwater resources. As such, 'KCB is a basin that bears the minimum surface water resources while owning the highest groundwater resources' as depicted by DMP (2015). Agricultural areas cover almost 55.5% of the basin followed by forests and semi-natural areas with 37.4% (CCIWR, 2016). The rest of land-use distribution is shared by urbanized areas and water surfaces. The region's agricultural production capacity has a strategic importance for Turkey's food supply, although KCB has the least amount of rainfall in the Central Anatolia (Celebi and Direk, 2017). KCB has a variety of surface water bodies as shown in Figure 1. Among the 17 water bodies 3 of them are lakes, whereas the rest are mainly wetlands of high ecological importance. 2 of them (Meke Maar and Kizoren Obrouk) have been declared as Ramsar sites. The area of each of these water bodies as well as their conservation status are given in Table 1.

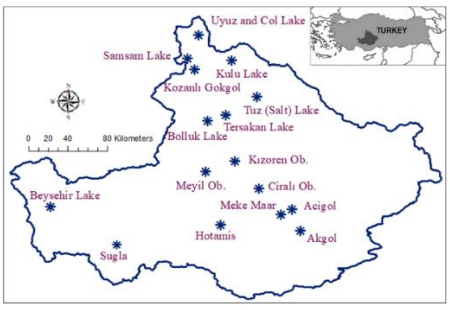

Figure.1 Geographical location of the surface water bodies in KCB

Table 1 Surface water bodies of KCB and their conservation status (Forestry Statistics, 2010; Url 1)

Name	Area (ha)	Conservation Status
Tuz Lake	240000	Natural Asset
Beysehir Lake	73000	Natural Asset Natural Park
Tersakan Lake	11000	Natural Asset
Akgol Wetland	5000	Natural Asset Nature Reserve
Bolluk Lake	3800	Natural Asset
Hotamis	5800	-
Kulu Lake	1800	Natural Asset
Col Lake	1500	-
Samsam Lake	830	Natural Asset
Acigol	400	-
Kozanli Gokgol	650	Natural Asset
Meke Maar	202	Natural Asset Nature Park Ramsar Site
Kizoren Obrouk	127	Ramsar Site
Cirali Obrouk	100	-
Meyil Obrouk	20	-
Uyuz Lake	15	Natural Asset

Musaoglu et al. (2018) conducted a long-term monitoring study of the wetlands in this basin via RS and Geographic Information System (GIS). The results derived indicated that the overall surface area of the water bodies in KCB decreased by approximately 23.5% within the inspection period of 1987-2017. One of the important wetlands of the basin named as Akgol Wetland has almost lost its water surface by 96% at the same time interval, and was in danger of extinction (Yagmur et al., 2018).

3. DATA AND METHODOLOGY

The flow diagram of the methodology developed specifically for this study is shown in Figure 2. The use of RS for KCB may be classified in 3 groups; field survey, satellite images, and ancillary data. Already available data and data produced within the scope of the study were placed under these 3 groups that formed the database of the basin. Data analyses were then realized with the gathered, produced and processed data stored in the database for watershed management. Apart from the methodology developed, ancillary data was also obtained during the site visits especially from the public authorities, regional institutions and more importantly, public advice and feedback were taken and utilized in the database formed. These details are not shown in the flow diagram of the methodology.

Field surveys consisted of spectroradiometer, GPS, levelling and thermal measurements; whereas, ancillary data was composed of watershed boundaries, meteorological data and digital elevation model (DEM) of the watershed. Optical and SAR images were both utilized. In this section, various examples on KCB will be presented under the available and produced data categories to enlighten the interested parties on the utilization and integration of RS in watershed management studies.

3.1 Available data

While conducting a study on a specific watershed, the primary work that should be realized is to delineate the watershed boundaries. It is important to fix the total area of concern at the beginning of the study. It is then that the topographical map of the watershed should be formed and illustrated in the form of DEM. Topography is an important component of resource inventory of a watershed. Figure 3 shows the example of DEM generated from SRTM for KCB.

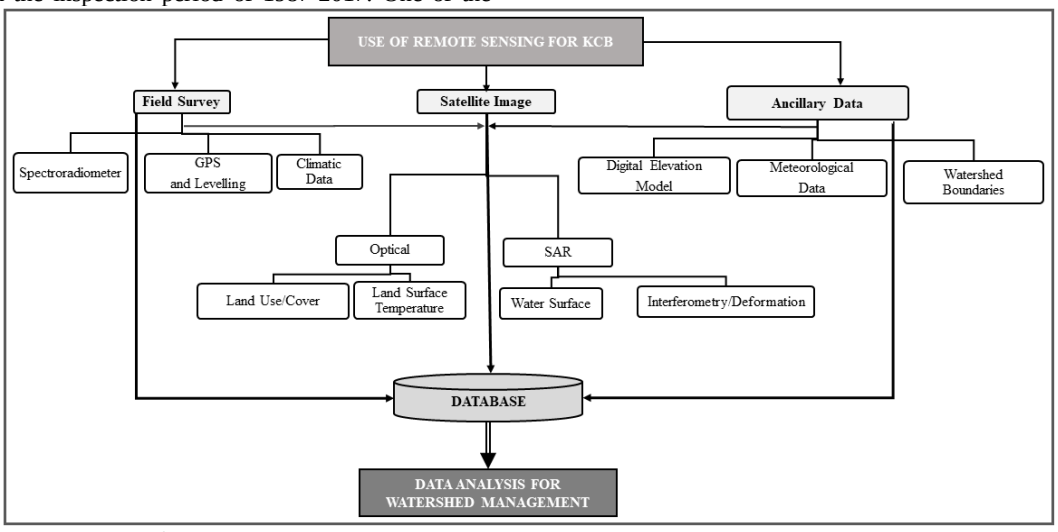

Figure.2 Flow chart of the methodology used

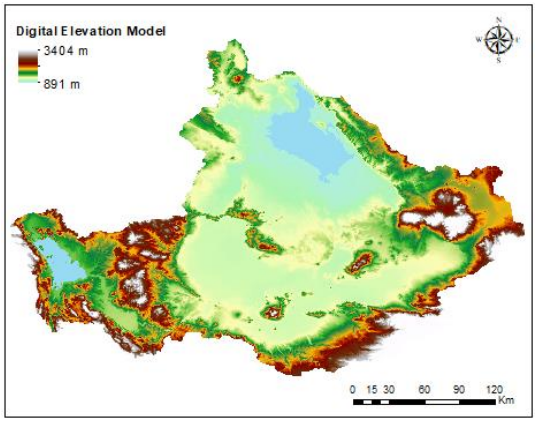

Figure.3 Digital Elevation Model (DEM) of KCB

The other available data that is of high importance in watershed management efforts is meteorological data including temperature, precipitation, evaporation, etc.

Required data were obtained from the nearest State Meteorological Station(s) representing the overall KCB. Figure 4 (a) and (b) demonstrate the long-term annual average temperature and precipitation values within the 1984-2017 period, respectively.

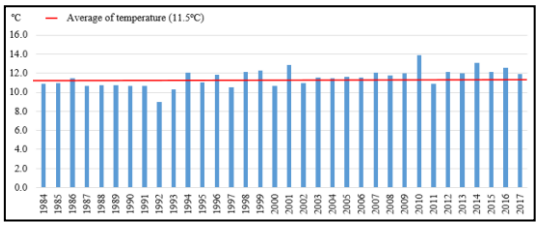

(a)

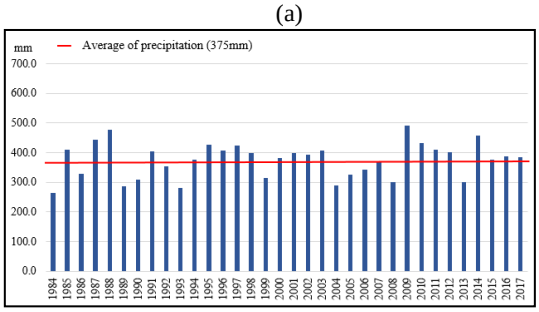

(b)

Figure.4 Long term annual average variation of (a) temperature and (b) precipitation values in KCB

As KCB is known as one of the most important agricultural areas of Turkey; dams have been built and put into operation for supplying the irrigation demand of the basin. In general, the basin bears an arid/semi-arid climatic character; and thus, suffers from water resources on the contrary to its fertile soil characteristics. Most of the water streams/rivers get dry during summer. Therefore, dry and hot summers accelerate evaporation leading to more water loss. For example, excess evaporation causes the formation of salt layers of almost 30 cm thickness during summer in the Tuz (Salt) Lake and water loss of the lake was further compensated by diverting water of another nearby water body, and by discharging the treated domestic wastewaters of Konya Province to the Lake via a main drainage channel. However, the situation in the 2 other systems, Meke Maar and Akgol Wetland was quite different. Water feeding and/or diversions from the other water resources have not been experienced so far leading to remarkable water losses. Areal values of the inspected water bodies were calculated from the satellite images at every 10-years interval between 1987-2017, whereas the meteorological data like temperature and precipitation were assessed starting from 1984. In the evaluation of the overall basin, data of the 12 meteorological stations existing in the basin were considered. However, only the nearby and representative ones were taken into consideration in discussing the climatic conditions of the individual water bodies. Meteorological data were gathered from the State Meteorological Service (SMS).

Hydrological condition of the watershed is also another important available data that can be depicted via RS. As referred in the introduction section, temporal and spatial assessments of water surfaces may be performed via satellite images belonging to various years. The areal values of water bodies are dynamic and are tend to change annually based on either natural and/or anthropogenic effects.

A noticeable areal change has occurred at Akgol Wetland, that is an internationally recognized water body of the basin, has almost lost its water surface by 96% during a period of 30 years (1987-2017), and thus, it is in danger of extinction (Musaoglu et al., 2018). This finding was the outcome derived from the various satellite images used belonging to different years.

3.2 Produced Data

3.2.1 Field Studies

Field spectroscopy is usually used to reach the reflectance information of field spectra. Spectroradiometer and GPS receiver were used to collect samples during the field surveys. FieldSpec HH is the model of spectroradiometer used with 325-1075 nm spectral range. Position and spectral reflectance of one of the samples from water is given in Figure 5 together with site photos taken during the field surveys. Sample referred in Figure 5 was taken from shallow water of Akgol Wetland. When Figure 5 is examined in depth, it will be seen that the properties of spectral signature of water can be observed. It has high reflectance in green region, whereas low reflectance in the NIR region. The spectral reflectance of a water area changes according to its depth and amount of materials present (McCoy, 2005).

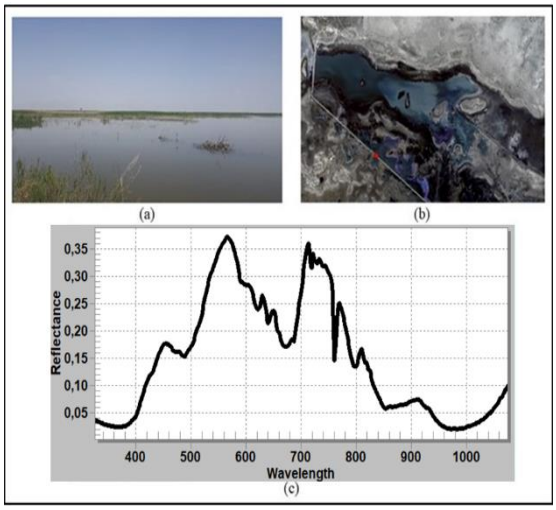

Figure.5 a) Water area, b) location of the water sample, c) spectral reflectance of the water sample

In addition, thermal measurements were also conducted in the study area with thermal thermometers providing extra data for evaluating the climatic condition of the basin. Produced LST from satellite images were also compared with field measurements (Sánchez-Aparicio et al., 2020).

Moreover, levelling at the basin was also carried out to calculate the accuracy of Sentinel 1 SAR interferometry results. During the field surveys, geometric levelling as one of the traditional measurement methods, was used to produce elevations in mm precision.

3.2.2 Remote Sensing

Resolution properties of satellite images enable information generation at different scales. It is possible to use different images based on the scale of the final product and on the required land-use/cover classes.

In this study, freely available MODIS, Landsat and Sentinel images were used for producing data at watershed with different scale. Moreover, Worldview-3 image was utilized to produce detailed information about Akgol Wetland. General characteristics of satellite images used and examples from different satellite images are given in Table 2 and Figure.6, respectively.

Table 2 Technical specifications of satellite data used

Sat.	Spatial Res.	Rad. Res.	Temp. Res.	Spectral Res. (µm)
MODIS	250m (bands 1-2) 500m (bands 3-7) 1000m (bands 8-36)	12 bit	16 days	36 bands: 1-19 from 0.620 to 0.965 20-36 from 3.66 to 14.28 microns
Landsat -5 TM	Red, Green, Blue, NIR, SWIR 1-2: 30 m TIR: 120 m	8 bit	16 days	Red :0,63-0.69 Green :0,52-0.60 Blue :0,45-0.52 NIR :0,76-0.90 SWIR 1:1.55-1.75 SWIR 2 :2.08-2.35
Landsat -8 OLI	Pan: 15 m Coastal, Cirrus, Red, Green, Blue, NIR, SWIR 1-2: 30 m TIR 1-2: 100 m	12 bit	16 days	Red :0,636-0.673 Green :0,533-0.590 Blue :0,452-0.512 NIR :0,851-0.879 SWIR 1:1.566-1.651 SWIR 2:2.107-2.294
Sentinel 2 MSI	Coastal, Water vapour, SWIR Cirrus: 60m Red, Green, Blue, NIR: 10 m Vegetation Red Edge, SWIR 1-2: 20 m	12 bit	5 days	Red :0,665 µm Green :0,560 µm Blue :0,490 µm NIR :0,842 µm SWIR 1:1.610 µm SWIR 2:2.190 µm
Worldview-3	Red, Red Edge, Coastal, Green, Yellow, Blue, NIR 1-2: 2 m	11 bit	By demand	Coastal: 0.40-0.45 Blue: 0.450-0.510 Green: 0.510-0.580 Yellow: 0.585-0.625 Red: 0.630-0.690 Red Edge: 0.705-0.745 NIR 1: 0.770-0.895 NIR 2: 0.860-1.040

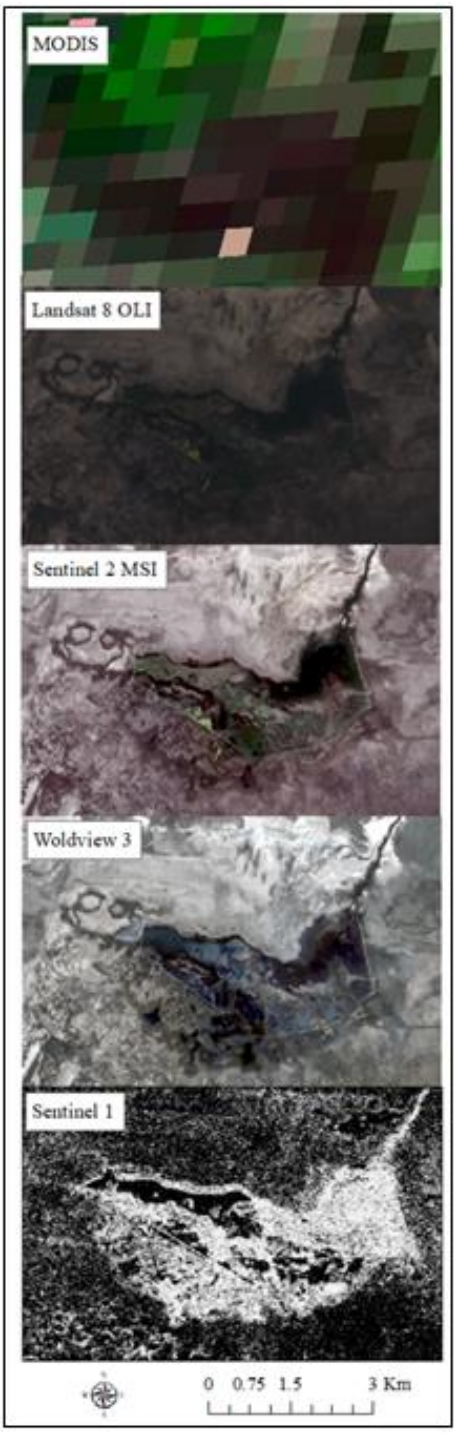

Figure.6 Satellite images used for Akgol Wetland

3.3 Methodology

3.3.1 Spectral Indices

Water surface area was calculated with Normalized Difference Water Index (NDWI). NDWI has been widely used for water body detection by Google Earth Engine software. Besides NDWI, there are various other water indices such as Modified NDWI, Automated Water Extraction Index (AWEI), and Water Ratio Index (WRI) etc. as mentioned in Table 3. Indices use different spectral bands of satellite images. For instance, NDWI uses green and near infrared bands of the satellite image and results vary between (-1) and (1). If results are greater than zero, they indicate the water areas. MNDWI (Modified Normalized Difference Water Index) detect water areas by preventing noises originating from built-up areas, soil and vegetation (Xu, 2006). AWEInsh is a suitable index to extract water areas which are not affected by high shadow. However, AWEIsh is a proper index to detect water areas under shadow effect (Feyisa et al., 2014). In addition, water areas can be detected by using WRI (Water Ratio Index). The values of the index greater than 1 show water covered area (Shen and Li, 2010).

Table 3. Spectral water indices used in this study

Index	Formula	Reference
NDWI	$\frac{(\text{Bgreen} - \text{Bnir})}{(\text{Bgreen} + \text{Bnir})}$	Mcfeeters (1996)
MNDWI	$\frac{(\text{Bgreen} - \text{Bswir})}{(\text{Bgreen} + \text{Bswir})}$	Xu (2006)
AWEIsh	$\text{Bblue} + 2.5 \times \text{Bgreen} - 1.5(\text{Bnir} + \text{Bswir1}) - 0.25 \times \text{Bswir2}$	Feyisa et al. (2014)
AWEInsh	$4 \times (\text{Bgreen} - \text{Bswir1}) - (0.25 \times \text{Bnir} + 2.75 \times \text{Bswir2})$	Feyisa et al. (2014)
WRI	$\frac{(\mathbf{Bgreen} + \mathbf{Bred})}{(\mathbf{Bnir} + \mathbf{Bswir1})}$	Shen and Li (2010)

3.3.2 Classification

Worldview-3 satellite image, which has high spatial and spectral resolution, was used in classification to achieve detailed information. Six classes in the region; deep water, shallow water, vegetation, agricultural area, soil and saline soil were discriminated by Worldview-3 satellite image. For that purpose, support vector machine (SVM) method was used. SVM is a nonlinear method used to generate an optimum hyperplane in high dimensional feature space (Vapnik, 1999).

The spectral bands; coastal, blue, green, yellow, red, red edge, NIR1, and NIR2 of the satellite image were used as features to generate a model. Samples were divided into train and test with K-fold cross validation method. In this method, the value of K parameter was chosen as 10.

A radial basis kernel was selected as kernel type and there were two hyper-parameters which were cost and gamma. The hyper-parameters were detected by grid search method, which was suggested by Hsu et al (2003) to find optimal hyper-parameters.

3.3.3 SAR processing

SAR images supply extended information about the physical properties more than the spectral properties of the earth. They can reflect the texture of the region. By using this feature of SAR images, surface water areas of lakes were automatically determined by using Google Engine. Sentinel-1 Ground Range Detected (GRD) products were calibrated by following the steps of thermal noise removal, radiometric calibration, terrain correction using digital elevation model, and converting backscatter values to decibels with Eq. 1.

$$\sigma 0(dB) = 10 \times \log 10\ \sigma^0 \quad (1)$$

Then, histogram-based image thresholding was applied on the image to extract water surface area.

3.4 Results

Five frequently used spectral indices shown in Table 3 were applied to Sentinel 2 image. Among these NDWI was selected as an example in this study. Therefore, it was applied to three different satellite images (MODIS, Landsat 8 and Sentinel 2). Figure 7 shows the results for KCB in 2018. Areal extents of the water bodies vary according to spatial resolution of the satellite images, and MODIS which has lower spatial resolution (500 m) showed lowest water area, whereas Sentinel 2 and Landsat 8 presented approximately the same water surface areas.

NDWI results of the Landsat images for overall KCB within years 1987-2017 is shown in Figure 8. It was seen that water surface area was decreased from 190517 ha to 134163 ha accounting to a decrease of approximately 30% between years 1987-2017. As such, the surface of water bodies varied from year to year, and this situation can be clearly observed from the multi-temporal illustration. Similar maps enable the quantification of the water amounts leading to calculations on the water budget of each and/or overall surface water bodies in the basin. These calculations are further utilized by the experts working on watershed management.

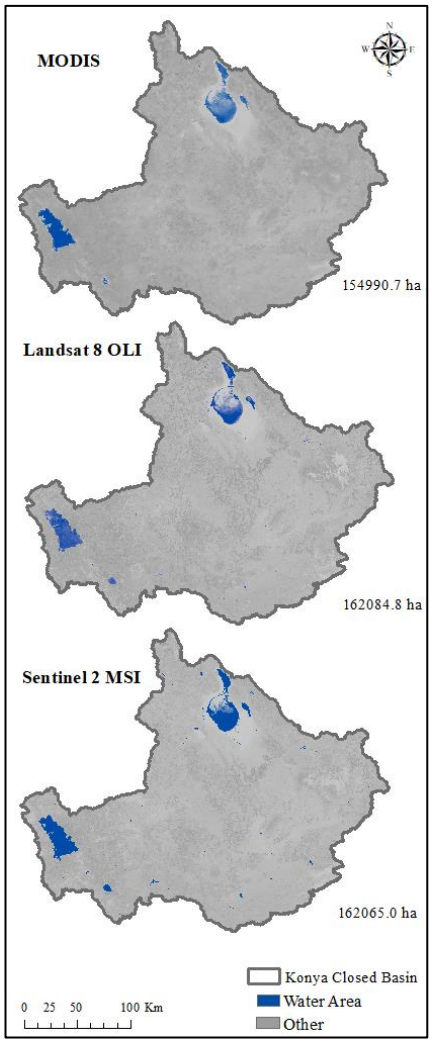

Figure.7 NDWI results of KCB with different satellite images

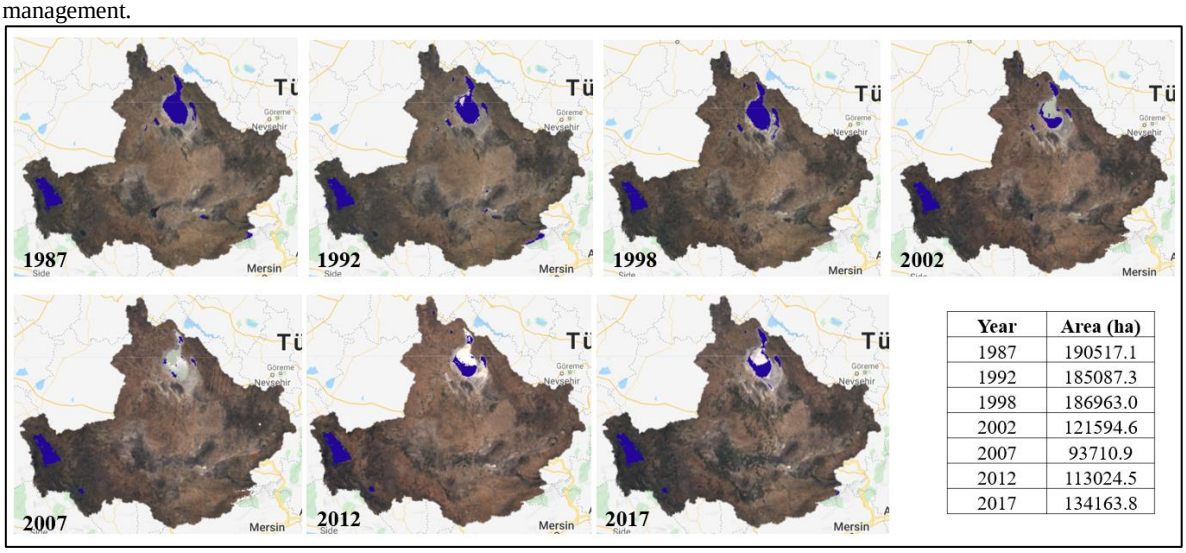

Year	Area (ha)
1987	190517.1
1992	185087.3
1998	186963.0
2002	121594.6
2007	93710.9
2012	113024.5
2017	134163.8

Figure.8 Long term changes of KCB between 1987-2017

Thematic map produced from Worldview-3 with SVM classifier is shown in Figure 9. Error matrix were generated and test data was used to calculate the overall accuracy. Overall accuracy of the map produced from Worldview-3 with SVM classifier is 96% and is shown in the Figure 10.

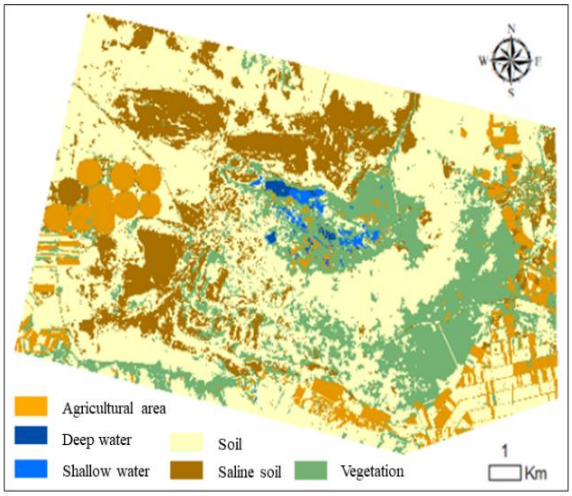

Figure.9 Thematic map produced from Worldview-3 with SVM classifier

User\Reference	Soil	Saline Soil	Vegetation	Agricultural area	Shallow water	Deep water	Sum
Soil	17805	0	0	7	320	0	18132
Saline soil	455	6749	0	0	0	0	7204
Vegetation	0	0	5877	18	0	0	5895
Agricultural area	0	0	641	13873	0	0	14514
Shallow water	0	0	0	0	7245	14	7259
Deep water	0	0	0	0	829	8423	9252
Sum	18260	6749	6518	13898	8394	8437	
Producer's accuracy	0.975	1	0.902	0.998	0.863	0.998	
User's accuracy	0.982	0.937	0.997	0.956	0.998	0.91	

Figure.10 Accuracy assessment results of classification

The sample results obtained with this code for Tuz Lake are shown in Figure 9. Surface water area variations can be observed on monthly basis in this figure. Therefore, one can easily determine the changes that occurs within different time lags. Additionally, interferometry pairs were generated by using Sentinel-1 images to determine the vertical changes of the wetlands and their surroundings.

Example for Tuz Lake is given in Figure 10. When the interferometry results are compared with levelling, a high positive correlation of 0.90 is obtained. This figure puts forth the changes on the water depths on monthly basis. Thus, a high positive correlation (r: 0.73) was calculated from the results obtained via Figure 11 and 12.

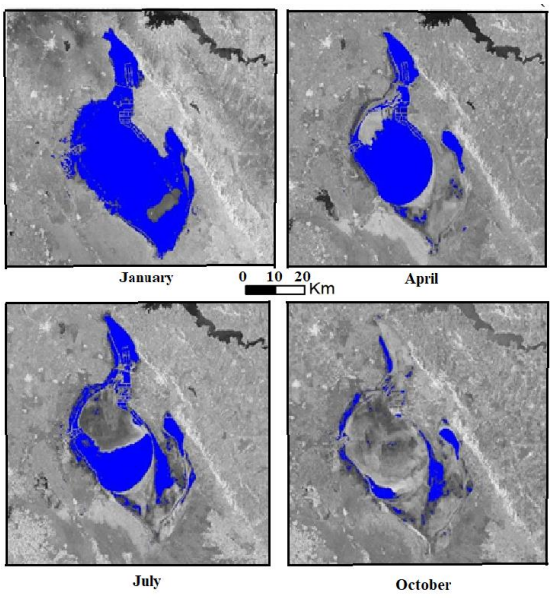

Figure.11 Monthly variations of recent water surfaces of Tuz Lake from Sentinel-1 SAR images (2018)

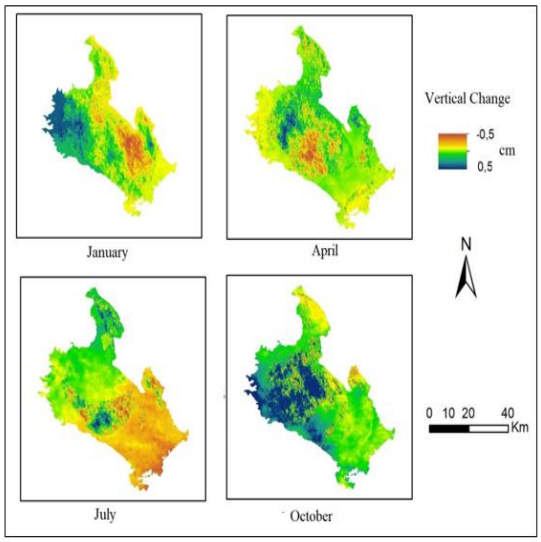

Figure.12 Vertical changes of Tuz Lake (2018)

4. CONCLUSION

As a conclusion, it can be stated that NDWI results of Sentinel 2 were more accurate than the others, especially MODIS because of its high spatial resolution. Landsat has been providing satellite images since 1970s. Therefore, it has been widely used for multi-temporal analysis. Besides Landsat, Sentinel 2 satellite image can also be used for watershed analysis that has higher resolution. For producing more detailed information, high resolution satellite image like Worldview-3 and classification algorithms can also be utilized. Sentinel 1 SAR images provide data under all weather conditions that is useful for seasonal monitoring.

Such integrated studies may be extended by adding the pollution criteria of both land and water bodies and by emphasizing on the social aspects of watershed

management in future works. It is important to note here that watersheds have dynamic structures as humans always appear at the center and govern many of the changes detected via RS technology.

All the referred and mentioned data provided with the use of RS are then stored in the database established to the watershed of concern. Further quarries, analyses, modelling, scenario analyses and development of management strategies can be realized. Integration of RS technology in watershed studies has gained an ever-increasing interest and highly favored by various disciplines.

ACKNOWLEDGEMENTS

The authors would like to acknowledge the financial support of the Scientific and Technological Research Council of Turkey under project number TUBITAK-116Y142, and also Istanbul Technical University (ITU) Scientific Projects Office (BAP) under project number MGA-2017-40803 and MYL-2018-41650.

REFERENCES

CCIWR. (2016). Climate Change Impact on Water Resources Project, Ministry of Forestry and Water Affairs, General Directorate of Water Management [Online]. Date of access: 21/04/2018 http://iklim.ormansu.gov.tr/Eng/

Celebi, M. and Direk, M. (2017). Farmer behaviours and sustainable water management in semiarid Konya Closed Basin in Turkey. International Journal of Advanced Biological and Biomedical Research, 6(1), pp. 441-450.

Comert, R, Matcı, D and Avdan, U (2019). Object based burned area mapping with random forest algorithm. International Journal of Engineering and Geosciences, 4 (2), 78-87. DOI: 10.26833/ijeg.455595

DMP. (2015). Konya Closed Basin Drought Management Plan Project, Ministry of Forestry and Water Affairs, General Directorate of Water Management. Date of access: 21/04/2018. http://www.suyonetimi.gov.tr.

Dursun, S., Onder, S., Acar, R., Direk, M. and Mucevher, O. (2012). Effect of environmental and socioeconomically change on agricultural production in Konya Region. Proceedings of International Conference on Applied Life Sciences (ICALS2012), Turkey, pp. 19-36.

EPA. (2008). Handbook for developing watershed plans to restore and protect our waters, United States Environmental Protection Agency, Office of Water Nonpoint Source Control Branch Washington, DC. EPA 841-B-08-002, March 2008.

Feyisa, G.L., Meilby, H., Fensholt, R. and Proud, S.R. (2014). Automated water extraction index: a new technique for surface water mapping using Landsat imagery. Remote Sensing of Environment, 140, pp. 23–35.

Forestry Statistics (2010). A Publication of Official Statistics Programme, Republic of Turkey Ministry of Forestry and Water Affairs, Ankara.

Heumann, B. W. (2011). An object-based classification of mangroves using a hybrid decision tree-Support vector machine approach. Remote Sensing, 3(11), 2440-2460.

Hsu, C.W., Chang, C.c. and Lin, C.J. (2003). A practical guide to support vector classification, Technical Report. Department of Computer Science and Information Engineering, University of National Taiwan, Taipei, 1–12.

Huang, C., Chen, Y., Zhang, S. and Wu, J. (2018). Detecting, extracting, and monitoring surface water from space using optical sensors: A review. Reviews of Geophysics, 56 (2), pp. 333-360.

Karakus, P., Karabork., H and Kaya, S. (2017). A comparison of the classification accuracies in determining the land cover of Kadirli region of Turkey by using the pixel based and object based classification algorithms. International Journal of Engineering and Geosciences, 2 (2), 52-60.

Lamb, B.T, Tzortziou, M. A. and McDonald, K. C. (2019). Evaluation of Approaches for Mapping Tidal Wetlands of the Chesapeake and Delaware Bays, Remote Sensing, 11 (20), 2366.

Li, L., Vrieling, A., Skidmore, A., Wang, T., Muñoz, A. AND Turak, E. (2015). Evaluation of MODIS Spectral Indices for Monitoring Hydrological Dynamics of a Small, Seasonally-Flooded Wetland in Southern Spain, Wetlands, 35, 851-864.

Ludwig, C., Walli, A., Schleicher, C., Weichselbaum, J. and Riffler, M. (2019). A highly automated algorithm for wetland detection using multi-temporal optical satellite data, Remote Sensing of Environment, 224, 333-351.

McCoy, R. M. (2005). Field methods in remote sensing, pp. 42-114, ISBN: 1593850808, Guilford Press, New York

McFeeters, S. K. (1996). The use of the normalized difference water index (NDWI) in the delineation of open water features. International Journal of Remote Sensing, 17(7), pp. 1425-1432.

Musaoglu, N. Tanik, A., Gumusay, U.M., Dervisoglu, A., Bilgilioglu, B.B., Yagmur, N, Bakırman, T., Baran, D. and Gokdag, F, M. (2018). Long-term monitoring of wetlands via remote sensing and GIS: a case study from Turkey, 2nd International Conference on Climate Change, Sri Lanka, Colombo, 15-16 February 2018, Proceedings Vol. 2, p. 11-21.

Randhir, O.T. (2007). Watershed Management- Issues and Approaches, IWA publishing, London, UK, p. 146.

Sánchez-Aparicio, M., Andrés-Anaya, P., Del Pozo, S. and Lagüela, S. 2020. Retrieving Land Surface Temperature from Satellite Imagery with a Novel Combined Strategy, 12, 277.

Shen, L. and Li, C. (2010), June. Water Body Extraction from Landsat ETM Imagery using Adaboost Algorithm. In Proceedings of the 18th International Conference on Geoinformatics, Beijing, China, pp. 1–4.

Tanik, A. (2019). Integrated watershed management. Lecture notes of CBM 546E graduate course at ITU Environmental Science, Engineering and Management Programme.

UN. (1997). Guidelines and manual on land-use planning and practices in watershed management and disaster reduction, United Nations, ST/ESCAP/1781, Economic and Social Commission for Asia and the Pacific, June 1997.

Url 1: http://www.kop.gov.tr/upload/dokumanlar/32.pdf (last accessed 1 April 2019)

Vapnik, V. (1999). The nature of statistical learning theory, pp. 133 – 140, ISBN: 0-387-98780-0, Springer science & business media, New York, Berlin, Heidelberg

Xu, H. (2006). Modification of normalized difference water index (NDWI) to enhance open water features in remotely sensed imagery. International Journal of Remote Sensing, 27(14), pp. 3025-3033.

Yagmur, N., Bilgilioglu, B.B., Musaoglu, N., Erten, E. and Tanik, A. (2018). Temporal changes of lentic system surfaces in Konya Closed Basin, Turkey, 3. ICOCEE 2018, 3rd International Conference on Civil and Environmental Engineering, İzmir, 24-27 April 2018, Conference E-Book Vol.2., pp. 658-668.

International Journal of Engineering and Geosciences (IJEG),
Vol; 5, Issue; 3, pp. 130-137, October, 2020,

International Journal of Engineering and Geosciences (IJEG),
Vol; 5, Issue; 3, pp. 130-137, October, 2020, *ISSN 2548-0960, Turkey,*
DOI: 10.26833/ijeg.644089

SPACE-BORNE AIR POLLUTION OBSERVATION FROM SENTINEL-5P TROPOMI: RELATIONSHIP BETWEEN POLLUTANTS, GEOGRAPHICAL AND DEMOGRAPHIC DATA

Gordana Kaplan [1]*, Zehra Yigit Avdan[2]

[1] Earth and Space Institute, Eskisehir Technical University, Eskisehir/Turkey;
(gkaplan@eskisehir.edu.tr) **ORCID 0000-0001-7522-9924**
[2] Department of Environmental Engineering, Eskisehir Technical University, Eskisehir/Turkey;
(zyigit@eskisehir.edu.tr); **ORCID 0000-0001-7445-3393**

*Corresponding Author, Received: 07/11/2019, Accepted: 11/01/2020

ABSTRACT: This study presents an analysis of the mean atmospheric column nitrogen dioxide (NO_2) and carbon monoxide (CO) over the Republic of North Macedonia during a six-month period. Measurements of NO_2 and CO obtained from the recently launched Sentinel-5 Precursor spacecraft with TROPOspheric Monitoring Instrument (Sentinel-5P TROPOMI) have been used. The aim of this study was to use relatively high-resolution satellite data for local air quality/air pollution monitoring and to investigate the relation of the pollutants with geographical and demographical data of the study area. For that purpose, along with CO and NO_2 data from TROPOMI, population statistics, digital elevation model and vegetation cover have been used for geo-spatial and statistical analyses. The findings show significantly high CO and NO_2 values in several parts of the study area, especially high CO values in the Vardar and Polog Valleys, and high NO_2 values in the densely populated cities. According to the analyses, there is high positive correlation between the NO_2 and the population statistics ($r = 0.78$; $R^2 = 0.61$) and high negative correlation ($r = -0.9$; $R^2 = 0.80$) between the altitude and the CO values of the study area. The overall results of this study confirmed the capability of Sentinel-5P TROPOMI data to be used in monitoring the air quality and air pollution over local areas.

Keywords: *Remote Sensing, Air pollution, Air quality, Population, Digital Terrain Model, Sentinel-5 TROPOMI.*

1. INTRODUCTION

With the rapid increase of the World`s population rises the problem of air pollution. One of the main causes of air pollution are urbanization, energy consumption, transportation, and motorization. Also, population growth and exposure to air pollutants have a negative impact on the quality of the environment and human health (Mayer 1999, Kampa and Castanas 2008, Hou et al. 2019). The World Health Organization (WHO) has identified air pollution as the single largest environmental health risk in the World (Organization 2016). Together with climate change, air pollution is one of the most serious threats to global health (Campbell-Lendrum and Prüss-Ustün 2019). It has been estimated that approximately four million people die every year as a result of exposure to air pollution in 2016, ambient air pollution has contributed to 7.6% of all deaths Worldwide (Organization 2016).

The biggest air pollutants encountered in our daily life are particulate matter (PM), sulfur dioxide (SO_2), nitrogen dioxide (NO_2), ozone (O_3), carbon monoxide (CO), and carbon dioxide (CO_2) (Chen et al. 2007). High concentrations of O_3, PM, and NO_2 near the Earth's surface can cause serious health problems, such as pulmonary and cardiovascular diseases (Brunekreef and Holgate 2002), and recognition is growing of the combined health effects of multiple pollutants (Dominici et al. 2010).

NO_2 is one of the largest components of urban air pollution and a precursor to ground-level O_3, PM, and acid rain (Bechle et al. 2013). The major source of NO_2 is the burning of fossil fuels such as coal, oil and gas. According to the European Environment Agency 2018 Air Quality report, more than 60% of the nitrogen dioxide in European cities comes from motor vehicle exhaust. Other sources of NO_2 are petrol and metal refining, electricity generation from coal-fired power stations, other manufacturing industries and food processing.

CO is a product of incomplete combustion as encountered in the operation of vehicles, heating, coal power generation, and biomass burning (Godish et al. 2014). Approximately 40% of CO comes from natural sources like volcanic eruptions, emission of natural gases, degradation of vegetation and animals, and forest fires (Varma et al. 2009), and 60% comes from fossil fuel consumption, garbage disposal, tobacco smoke, and charcoal fires (Vreman et al. 2000). Although tropospheric CO is not regarded as a health concern outdoors, recent studies show a possible link between exposure to urban CO concentrations and cardiac problems (Andre et al. 2010). Satellite observations of tropospheric NO_2 have been conducted since 1995 (Burrows et al. 1999) with the Global Ozone Monitoring Experiment (GOME) satellite instrument, designed to observe the several gases in the Earth`s stratosphere and troposphere.

For a reliable prediction and decision-making to mitigate the impact of air pollutants, continuous and accurate monitoring of the air quality is necessary (Hou, Wang et al. 2019). In comparison with conventional measurements, remote sensing techniques and Geo-Information Systems (Guo et al. 2019) are capable of providing complementary information for unmonitored areas (Theys et al. 2019) and for acquiring information about the Earth such as Land and Sea Surface Temperature (Khorrami et al. 2019, Nacef et al. 2016), vegetation cover, air quality and even predict and evaluate natural disaters such as fires (Comert et al. 2019). Satellite observation for air quality have been used for over four decades starting with the launch of the Total Ozone Monitoring Instrument (TOMS) in 1978, GOME in 1995 (Burrows et al. 1999), Ozone Monitoring Instrument (OMI) in 2004, and Sentinel-5 Precursor Tropospheric monitoring instrument (Sentinel-5P TROPOMI) in 2017. These satellite instruments are designed to observe the several gases in the Earth`s stratosphere and troposphere. For example, Jabeen et al. (Jabeen and Khokhar 2019) used low-spatial resolution OMI satellite data for monitoring the atmospheric burdens of SO_2 over Pakistan over a time period of 2005–2016, while Hou et al. (Hou et al. 2019) used OMI satellite data for investigating the temporal and spatial dynamics of NO_2 over China. Similar, Oner et al. (Oner and Kaynak 2016) evaluated the NO_x emissions from available inventories using satellite NO_2 retrievals from OMI over Turkey. Deferring from the other air-quality observation satellite instruments, TROPOMI has a relatively high spatial resolution that is necessary for air quality applications (Abida et al. 2016). Since the launch of Sentinel-5p, several studies have shown the success of the TROPOMI instrument. Thus, Kaplan et al. (Kaplan et al. 2019), used TROPOMI data for monitoring the NO_2 over Turkey, Theys et al. (Theys et al. 2019) investigated volcanic SO_2, and Borsdorff et al. (Borsdorff et al. 2018) presented the first results of measuring CO with TROPOMI over China. Statistical analyses of the global comparison between TROPOMI and ground-based measurements show small percentage difference (Garane et al. 2019). This study investigates the relationship between air pollutants, geographical and demographical data using high-resolution space-borne data retrieved from the TROPOMI sensor over a six-month period over the Republic of North Macedonia. Using high-resolution Sentinel-5p imagery, the main objectives of this study are:

- Estimating the NO_2 and CO amount over the Republic of North Macedonia;
- Determining the relationship between the demographic data and air pollutants;
- Determining the relationship between geographical data and air pollutants.

2. DATA AND METHODS

2.1 Study Area

The Republic of North Macedonia (41.6086° N, 21.7453° E) is a landlocked country within the Balkan Peninsula in Southeast Europe (Figure 1), with a total area of 25.713 km^2. The countries geography consists of mountains, valleys, and rivers, defined by a central valley formed by the Vardar river framed by mountain ranges with sixteen mountains higher than 2,000 meters above sea level.

Figure 1. Study Area; Republic of North Macedonia

Based on the latest United Nations estimates, Macedonia has 2.086.815 inhabitants. The city of Skopje, formed on the riverbed of Vardar, is the capital with more than 500.000 of 2.08 million inhabitants. North Macedonia has a transitional Mediterranean to continental climate.

In the past few years, the air quality in the country is a cause of serious concern as the limit values set for the protection of human health are significantly exceeded. According to the Macedonian Air Quality Assessment Report for 2005-2015, air pollution is on high level in the largest urban settlements, especially in the city of Skopje and Tetovo, where the NO_2 and CO have exceeded the limit values of 40 µm/m^3 for NO2 at annual, and 10 µm/m^3 at daily period. As one of the main air polluters are considered to be household heating, population density, transportation, industry, and urbanization. The national air quality monitoring network includes 17 stations in different parts of the country measuring SO_2, CO, NO_2, O_3 and PM. According to the Air quality in Europe - 2018 report (Agency 2018), the annual limit value of air pollutants in 2016 has been above the limited values.

2.1 Data and Methods

TROPOMI is a space-borne spectrometer covering wavelength bands between the ultraviolet and the shortwave infrared, and it is the single payload of the Sentinel-5p spacecraft launched 13th October 2017 into the low earth orbit funded jointly by the Netherlands Space Office and the European Space Agency (ESA). The data has open access and it can be downloaded from the ESA Copernicus Open Access Hub (https://scihub.copernicus.eu/). The instrument is designed to obtain data for air quality and climate observations (Voors, de Vries et al. 2017). The instrument operates in a push-broom configuration (non-scanning), with a swath width of approximately 2600 km on the Earth's surface which makes daily global coverage in combination with good spatial resolution possible. No additional pre-processing is required before using the data.

Using spectral bands from the ultraviolet, visible and near-infrared wavelength range, TROPOMI measures O_3, NO_2, SO_2, bromate (BrO_3^-), formaldehyde (HCHO) and water vapor (H_2O) tropospheric columns from the ultraviolet, visible and near-infrared wavelength, and CO and methane (CH_4) tropospheric columns are measured from the short-wave infrared wavelength range (Veefkind, Kleipool et al. 2017) (Table 1).

Table 1. Summary of the TROPOMI spectral bands and their key features (Veefkind, Kleipool et al. 2017)

Band		Spectral coverage [nm]	Swath width [km]	Spectral resolution [nm]	Temporal resolution	Spatial sampling [km^2]
UV	1	270 – 320	~2600	0.49	Daily	7x28
	2					7x3.5
VIS	3	320 – 495		0.54		
	4					
NIR	5	675 – 775		0.38		
	6					
SWIR	7	2305 – 2385		0.25		7x7
	8					

In comparison with the other existing air quality observing space-borne instruments, TROPOMI's much finer spatial resolution promises to improve substantially of the information content. TROPOMI is the first imaging spectrometer ever to deliver global data with a moderate spatial resolution and a continuous spectral sampling of the red and NIR spectral regions (the so-called vegetation red-edge), which are also covered by GOME-2 but with a much coarser spatial resolution. (Guanter et al. 2015).

With the theoretical fact that there is a high relation between the altitude and air pollution density (Müezzinoğlu 1987), several studies have investigated the relationship between altitude and air quality, and have reported that air pollution declines with height (Ji et al. 2018). However, there is insufficient evidence to support significantly increased ecological effects and dispersion change at high altitudes.

Taking into consideration the advantages of the TROPOMI instrument, this paper investigates the relationship between air pollutants, geographical and demographical data using high-resolution space-borne data over a six-month period over the Republic of North Macedonia. The mean value of the NO_2 and CO collected from July 2018 to January 2019 were compared with the geographical and demographic data (Figure 2) from the study area. Thus, a satellite retrieved digital terrain model (DTM) and a vegetation cover map, , were used for a statistical relationship with the air pollutants (Figure 3).

A NDVI from MODIS with an approximate spatial resolution of 1 km was used in this study. In order to be able to compare the data, the NDVI resolution has been decreased to TROPOMI`s resolution. Same was the case for the 90 m DTM from the satellite ASTER.

The summary and maximum value of the air pollutants, CO and NO_2, were statistically calculated for thirty-four municipalities in North Macedonia, separately. Accordingly, the same calculations were made for geographical and vegetation data. Using geospatial analyses, the remote sensing data were linked to the demographical statistics and afterward, statistical analyses were performed.

In a campaign carried by the Finish Meteorological Institute and the Royal Netherlands Meteorological Institute during April-September 2018 (Ialongo et al. 2018), TROPOMI data were compared with ground-based observation in Helsinki. According to the findings, it was concluded that the differences between the total columns derived from the TROPOMI and Pandora instruments are on average less than 10 %.

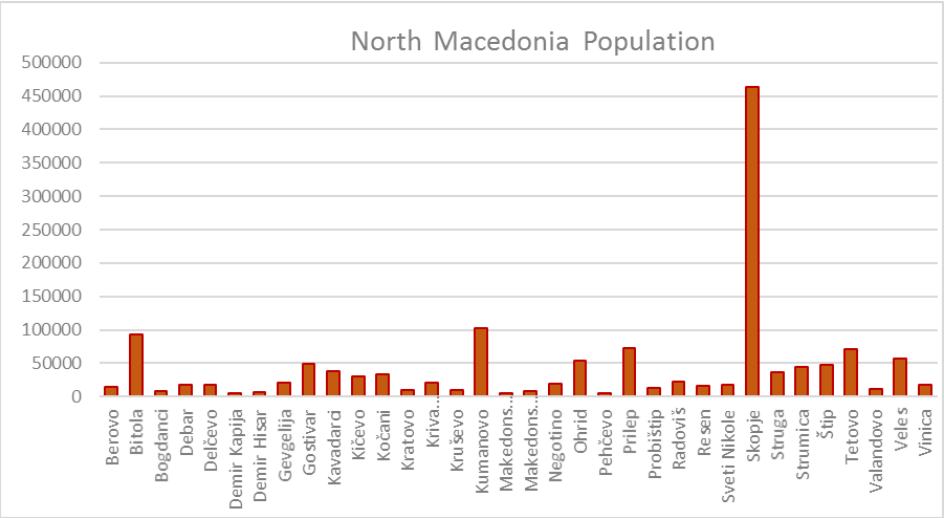

Figure 2. North Macedonia population

the

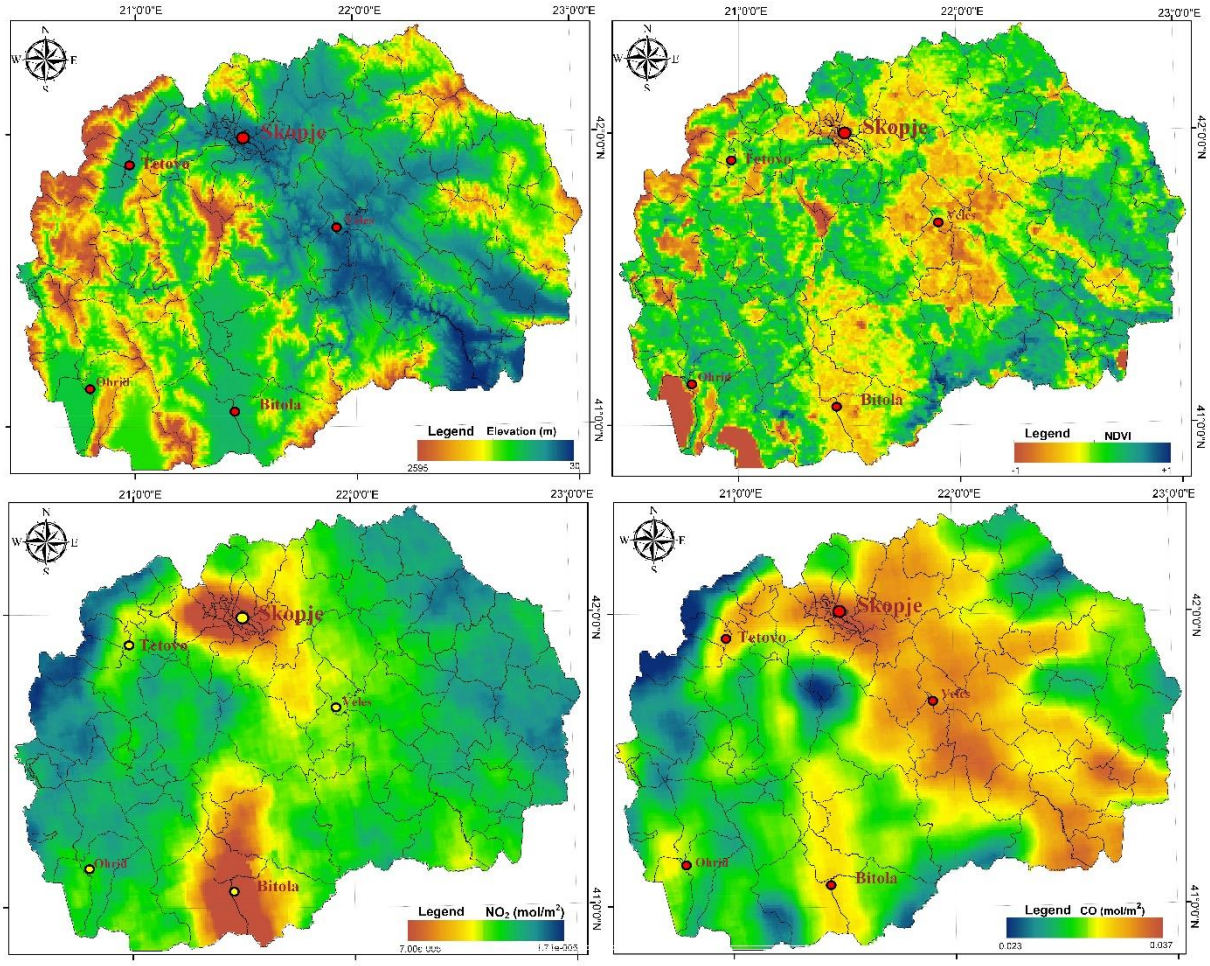

Figure 3. Remote Sensing data used in this study

3. RESULTS AND DISCUSSION

3.1 Overall results of CO and NO_2

The spatial distribution of tropospheric CO and over the Republic of North Macedonia during July 2018 – January 2019 are presented in Figure 4. The selected period is from summer, autumn and winter. Observing both visual (Figure 3) and statistical results of CO, it can be noticed that several regions have significantly higher values than others. Thus, high values can be noticed in the cities of Skopje, with highest value of 0.036 mol/km^2, Strumica, Negotino, Kavadarci, Gevgelija, Demir Kapija, and Veles, respectively. If seen geographically, it can be noticed that the highest CO values are set in the Vardar Valley. Other than that, high CO values can be also noticed in the Polog Valley, in the cities Prilep and Bitola, respectively.

Figure 5 shows the spatial distribution of tropospheric NO_2 over the Republic of North Macedonia from July 2018 – January 2019. Observing both visual (Figure 3) and statistical results of NO_2, it can be noticed that several regions have significantly higher values than others. Thus, high values can be noticed in the cities of Skopje, with highest value of 7.0*10^{-5} mol/km^2, Bitola 6.0*10^{-5} mol/km^2, Prilep 5.0*10^{-5} mol/km^2, Kumanovo 4.0*10-5 mol/km^2, respectively. It should be noticed that these are cities with highest population statistics.

3.2 Relationship Between Pollutants, Geographical and Demographical Data

Although the relationship between pollutants and other factors is generally known, further investigation is needed. Several studies have investigated the relationship between altitude and air quality, and have reported that air pollution declines with height (Ji et al. 2018). However, there is insufficient evidence to support significantly increased ecological effects at high altitudes. In order to mitigate air pollution and to increase air quality, firstly the biggest contributors and causes of air pollution need to be detected. In this study, the relation between several air pollutants, CO and NO_2, and demographical and geographical data have been statistically analyzed. For that purpose, coefficient of determination and correlation coefficients have been retrieved, and the results of the correlation between the NO_2 and the population statistics are presented in Figure 6 from where a high correlation between the population and both maximum value and summary of the NO2 can be noticed. Thus, it can be concluded that in more than 60% of the cases, the NO2 value will increase if the population increases and vice versa (Figure 6). These results are expected, as the major source of NO_2 is the burning of fossil fuels such as coal, oil and gas.

Figure 4. Mean tropospheric CO obtained from TROPOMI over North Macedonia from July 2018 to January 2019

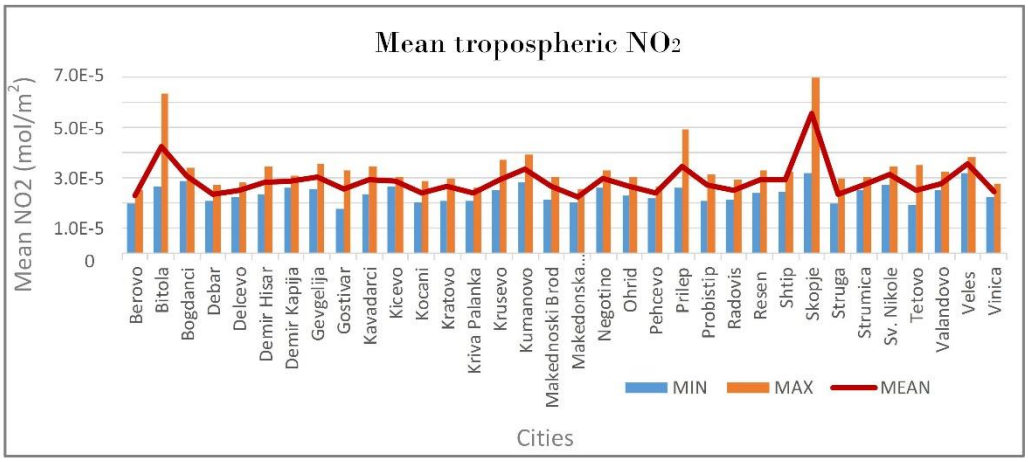

Figure 5. Mean tropospheric NO2 obtained from TROPOMI over North Macedonia from July 2018 to January 2019

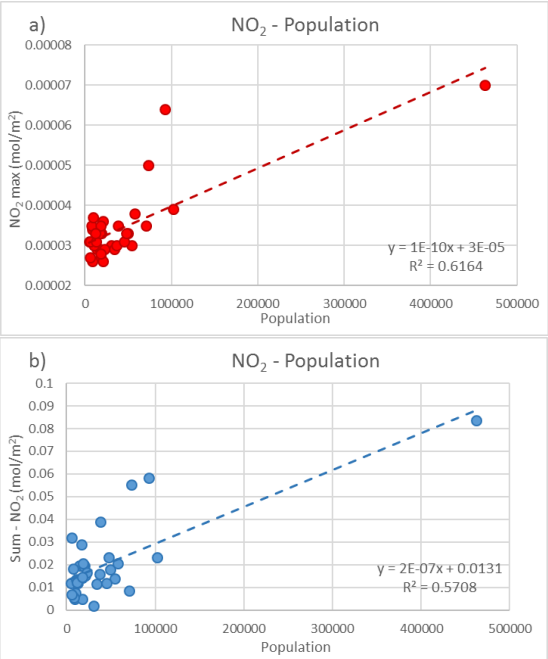

Figure 6. Mean values of tropospheric NO_2 obtained from TROPOMI over North Macedonia from July 2018 to January 2019 and statistical correlation with; a) maximum NO2 value; b) summary of NO_2

Although no significant relation could be found between the CO and the population statistics, the results showed that CO values are highly correlated with the elevation of the area. This can be also seen in Figure 3 where high CO values are noted along Vardar Valley followed by high values in the Polog valley. Thus, the correlation coefficient between the CO and the DTM shows high negative correlation (r = -0.9; R^2 = 0.8), meaning that 80% of the times, as the altitude rises, the CO value will decrease. Also, an analysis between the two air pollutants was made and the results showed a medium positive correlation (r = 0.51) between CO and NO_2. The correlation values between the air pollutants, geographical and demographical data can be seen in Figure 7.

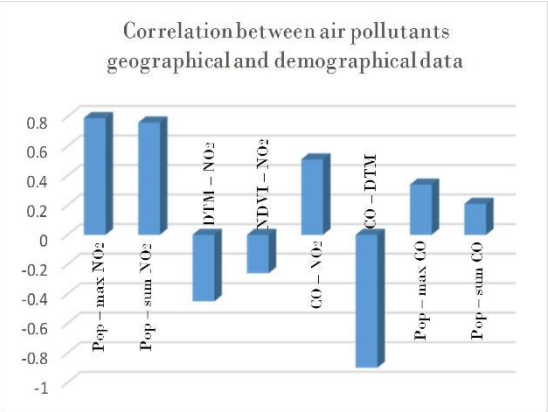

Figure 7. Correlation coefficients between air pollutants obtained from TROPOMI and geographical and demographical data

4. CONCLUSION

In this study, the relation between air pollutants, CO and NO_2 remotely sensed data retrieved from the Sentinel-5P TROPOMI instrument over the Republic of North Macedonia during the period July 2018 – January 2019, and geographical and demographical data has been investigated. In comparison with the other existing air quality observing space-borne instruments, with TROPOMI's much finer spatial resolution, in this study detailed investigation of the air quality in every municipality was made. Furthermore, using remote sensing, geo-spatial analyses and statistical analyses, the relation between the North Macedonia`s population statistics, altitude values extracted from a DTM, vegetation cover, and mean values over a six-month period of CO and NO_2 have been made. The results from this study can be summarized as follows:

1) Both visual and statistical results of CO indicate that several regions have higher values than others. Significantly high values can be noticed in the Vardar and Polog Valley;

2) From the NO_2 observation, high values can be noticed in the cities with highest population; Skopje, with a highest value of 7.0*10-5 mol/km^2, Bitola, Prilep, Kumanovo, respectively;

3) The coefficient of determination and correlation coefficients indicates high correlation between the NO_2 and the population statistics (r = 0.78; R^2 = 0.61);

4) The results showed high negative correlation (r = -0.9; R^2 = 0.8) between the altitude of the study area and the CO values.

The overall results of this study confirm the capability of Sentinel-5P TROPOMI data to be used in monitoring the air quality and air pollution over local areas. In this study, analyses were made separately for thirty-four municipalities. Monitoring the air quality with ground measurements can be challenging and insufficient as there is limited number of air-quality monitoring stations. With TROPOMI data, air quality information can be obtained daily with a relatively high spatial resolution.
Compared with the Macedonian Air Quality Assessment Report for 2005-2015, the results are with good correlation, as the report also indicates that air pollution is on high level in the largest urban settlements, especially in the city of Skopje and Tetovo, where the NO_2 and CO have exceeded the limit values of 40 µm/m3 for NO2 at annual and 10 µm/m3 at daily period.

For future studies, we recommend investigating the seasonal variation of the pollutants observed with the TROPOMI instrument, exploring other pollutants, validating the results with ground measurements, and evaluating other factors such as wind direction, building density or other factors that may contribute to air pollution.

REFERENCES

Abida, R., L. El Amraoui, P. Ricaud, W. Lahoz, H. Eskes, A. Segers, L. Curier, J. de Haan, A. Nijhuis and D. Schuettemeyer (2016). "Impact of Spaceborne Carbon Monoxide Observations from the S-5P platform on Tropospheric Composition Analyses and Forecasts." Atmospheric Chemistry and Physics 2016 (2): 1-1.

Agency, E. E. (2018). "Air quality in Europe — 2018 report." Available at: https://www.eea.europa.eu › air-quality-in-europe-2018. Access date: 10.11.2019

Andre, L., J. Boissière, C. Reboul, R. Perrier, S. Zalvidea, G. Meyer, J. Thireau, S. Tanguy, P. Bideaux and M. Hayot (2010). "Carbon monoxide pollution promotes cardiac remodeling and ventricular arrhythmia in healthy rats." American journal of respiratory and critical care medicine 181(6): 587-595.

Bechle, M. J., D. B. Millet and J. D. Marshall (2013). "Remote sensing of exposure to NO2: Satellite versus ground-based measurement in a large urban area." Atmospheric Environment 69: 345-353.

Borsdorff, T., J. Aan de Brugh, H. Hu, I. Aben, O. Hasekamp and J. Landgraf (2018). "Measuring carbon monoxide with TROPOMI: First results and a comparison with ECMWF‐IFS analysis data." Geophysical Research Letters 45(6): 2826-2832.

Brunekreef, B. and S. T. Holgate (2002). "Air pollution and health." The lancet 360(9341): 1233-1242.

Burrows, J. P., M. Weber, M. Buchwitz, V. Rozanov, A. Ladstätter-Weißenmayer, A. Richter, R. DeBeek, R. Hoogen, K. Bramstedt and K.-U. Eichmann (1999). "The global ozone monitoring experiment (GOME): Mission concept and first scientific results." Journal of the Atmospheric Sciences 56(2): 151-175.

Campbell-Lendrum, D. and A. Prüss-Ustün (2019). "Climate change, air pollution and noncommunicable diseases." Bulletin of the World Health Organization 97(2): 160.

Chen, T.-M., W. G. Kuschner, J. Gokhale and S. Shofer (2007). "Outdoor air pollution: nitrogen dioxide, sulfur dioxide, and carbon monoxide health effects." The American journal of the medical sciences 333(4): 249-256.

Çömert, Resul, DİLEK KÜÇÜK, and Uğur Avdan. "OBJECT BASED BURNED AREA MAPPING WITH RANDOM FOREST ALGORITHM." International Journal of Engineering and Geosciences 4.2: (2019) 78-87.

Dominici, F., R. D. Peng, C. D. Barr and M. L. Bell (2010). "Protecting human health from air pollution: shifting from a single-pollutant to a multi-pollutant approach." Epidemiology (Cambridge, Mass.) 21(2): 187.

Garane, K., M.-E. Koukouli, T. Verhoelst, V. Fioletov, C. Lerot, K.-P. Heue, A. Bais, D. Balis, A. Bazureau and A. Dehn (2019). "TROPOMI/S5ptotal ozone column data: global ground-based validation & consistency with other satellite missions."

Godish, T., W. T. Davis and J. S. Fu (2014). Air quality, CRC Press.

Guanter, L., I. Aben, P. Tol, J. Krijger, A. Hollstein, P. Köhler, A. Damm, J. Joiner, C. Frankenberg and J. Landgraf (2015). "Potential of the TROPOspheric Monitoring Instrument (TROPOMI) onboard the Sentinel-5 Precursor for the monitoring of terrestrial chlorophyll fluorescence." Atmospheric Measurement Techniques 8(3): 1337-1352.

Guo, L., J. Luo, M. Yuan, Y. Huang, H. Shen and T. Li (2019). "The influence of urban planning factors on PM2. 5 pollution exposure and implications: A case study in China based on remote sensing, LBS, and GIS data." Science of The Total Environment 659: 1585-1596.

Hou, Y., L. Wang, Y. Zhou, S. Wang, W. Liu and J. Zhu (2019). "Analysis of the tropospheric column nitrogen dioxide over China based on satellite observations during 2008–2017." Atmospheric Pollution Research 10(2): 651-655.

Ialongo, I., H. Virta, H. Eskes, J. Hovila and J. Douros (2018). "Comparison of TROPOMI/Sentinel 5 Precursor NO2 observations with ground-based measurements in Helsinki."

Jabeen, Z. and M. F. Khokhar (2019). "Extended database of SO2 column densities over Pakistan by exploiting satellite observations." Atmospheric Pollution Research 10(3): 997-1003.

Ji, H., S. Chen, Y. Zhang, H. Chen, P. Guo and P. Zhao (2018). "Comparison of air quality at different altitudes from multi-platform measurements in Beijing." Atmospheric Chemistry and Physics 18(14): 10645-10653.

Kampa, M. and E. Castanas (2008). "Human health effects of air pollution." Environmental pollution 151(2): 362-367.

Kaplan, G., Z. Y. Avdan and U. Avdan (2019). Spaceborne Nitrogen Dioxide Observations from the Sentinel-5P TROPOMI over Turkey. Multidisciplinary Digital Publishing Institute Proceedings.
Mayer, H. (1999). "Air pollution in cities." Atmospheric environment 33(24-25): 4029-4037.

Khorrami, Behnam, et al. "Land surface temperature anomalies in response to changes in forest cover." International Journal of Engineering and Geosciences 4.3 (2019): 149-156.

Müezzinoğlu, A. (1987). "Air Pollution and Quality, in Turkish " Dokuz Eylül Üniversitesi Mühendislik Mimarlık Fakültesi Ders Notu MM/ÇEV-87 EY 127.

Nacef, Lamri, et al. "Variability and decadal evolution of temperature and salinity in the mediterranean sea surface." International Journal of Engineering and Geosciences 1.1 (2016): 20-29.

Oner, E. and B. Kaynak (2016). "Evaluation of NOx emissions for Turkey using satellite and ground-based observations." Atmospheric Pollution Research 7(3): 419-430.

Organization, W. H. (2016). "Ambient air pollution: A

global assessment of exposure and burden of disease." Available at: https://www.who.int › phe › publications › air-pollution-global-assessment Access date: 05.12.2019

Theys, N., P. Hedelt, I. De Smedt, C. Lerot, H. Yu, J. Vlietinck, M. Pedergnana, S. Arellano, B. Galle and D. Fernandez (2019). "Global monitoring of volcanic SO 2 degassing with unprecedented resolution from TROPOMI onboard Sentinel-5 Precursor." Scientific reports 9(1): 2643.

Varma, D. R., S. Mulay and S. Chemtob (2009). Carbon monoxide: from public health risk to painless killer. Handbook of toxicology of chemical warfare agents, Elsevier: 271-292.

Veefkind, J. P., Q. Kleipool, A. Ludewig, D. Stein-Zweers, I. Aben, J. De Vries, D. G. Loyola, H. Nett, A. Richter and M. Van Roozendael (2017). Early Results from TROPOMI on the Copernicus Sentinel 5 Precursor. AGU Fall Meeting Abstracts.

Voors, R., J. de Vries, I. S. Bhatti, D. Lobb, T. Wood, N. van der Valk, I. Aben and P. Veefkind (2017). TROPOMI, the Sentinel 5 Precursor instrument for air quality and climate observations: status of the current design. International Conference on Space Optics—ICSO 2012, International Society for Optics and Photonics.

Vreman, H. J., R. J. Wong and D. K. Stevenson (2000). "Carbon monoxide in breath, blood, and other tissues." Carbon monoxide toxicity: 19-60.

International Journal of Engineering and Geosciences (IJEG),
Vol; 5, Issue; 3, pp. 138-143, October, 2020, ISSN 2548-0960, Turkey,
DOI: 10.26833/ijeg.645426

FEATURE EXTRACTION FROM SATELLITE IMAGES USING SEGNET AND FULLY CONVOLUTIONAL NETWORKS (FCN)

Batuhan Sariturk[1]*, Bulent Bayram[2], Zaide Duran[1], Dursun Zafer Seker[1]

[1] Istanbul Technical University, Faculty of Civil Engineering, Department of Geomatics Engineering, Istanbul, Turkey (sariturkb/duranza/seker@itu.edu.tr); **ORCID 0000-0001-8777-4436, ORCID 0000-0002-1608-0119, ORCID 0000-0001-7498-1540**

[2] Yildiz Technical University, Faculty of Civil Engineering, Department of Geomatics Engineering, Istanbul, Turkey (bayram@yildiz.edu.tr); **ORCID 0000-0002-4248-116X**

*Corresponding Author, Received: 00/XX/201X, Accepted: 00/XX/201X

ABSTRACT: Object detection and classification are among the most popular topics in Photogrammetry and Remote Sensing studies. With technological developments, a large number of high-resolution satellite images have been obtained and it has become possible to distinguish many different objects. Despite all these developments, the need for human intervention in object detection and classification is seen as one of the major problems. Machine learning has been used as a priority option to this day to reduce this need. Although success has been achieved with this method, human intervention is still needed. Deep learning provides a great convenience by eliminating this problem. Deep learning methods carry out the learning process on raw data unlike traditional machine learning methods. Although deep learning has a long history, the main reasons for its increased popularity in recent years are; the availability of sufficient data for the training process and the availability of hardware to process the data. In this study, a performance comparison was made between two different convolutional neural network architectures (SegNet and Fully Convolutional Networks (FCN)) which are used for object segmentation and classification on images. These two different models were trained using the same training dataset and their performances have been evaluated using the same test dataset. The results show that, for building segmentation, there is not much significant difference between these two architectures in terms of accuracy, but FCN architecture is more successful than SegNet by 1%. However, this situation may vary according to the dataset used during the training of the system.

Keywords: *Photogrammetry, Deep Learning, Feature Extraction, SegNet, Fully Convolutional Networks*

1. INTRODUCTION

Building detection from remote sensing and photogrammetric images has been one of the most challenging tasks with important development and research efforts during recent years (Vakalopoulou et al., 2015). In remote sensing field, applications such as urban planning, land cover/use analysis and automatic generation or updating of the maps, along with the detection of buildings, are long-standing problems (Wu et al., 2018a).

Buildings, which are the most significant places for human life, are key elements in the mapping of urban areas (Chen et al., 2019). Due to the rapid changes in urban areas, it is important to create and update the location information of buildings (Wu et al., 2018b). Remote sensing has been an effective technology for accurate detection and mapping of buildings due to its capability for high-resolution imaging over large areas and advantages of fast and high accuracy data acquisition (Chen et al., 2019, Comert et al., 2019). Unfortunately, automatic building detection on aerial images is usually limited by the inadequate detection and segmentation accuracy (Chen et al., 2019). Most tasks still require great amounts of manual interventions by experts.

In recent years, as a consequence of the developments of imaging sensors and corresponding platforms, a rapid increase in the availability and accessibility of very high-resolution (VHR) remote sensing images has made this problem more and more urgent (Ma et al., 2017). In the literature, satellite images have been used widely for the classification of urban areas (Sevgen, 2019). Building extraction from satellite and aerial images is not an easy task because of complex backgrounds, different lightning conditions and external factors that reduce visibility or separability of buildings (Akbulut et al., 2018).

Recent progress in the field of computer vision (CV) indicates that, with the help of sufficient computing power and large training datasets (Cordts et al., 2016; Deng et al., 2009; Everingham et al., 2010; Lin et al., 2014), deep learning methods such as Convolutional Neural Networks (CNNs) (LeCun et al., 1989) can considerably improve the performance of object detection and segmentation tasks from high-resolution imagery (He et al., 2016; Krizhevsky et al., 2012). Neural networks can deal with complex problems to reach accurate solutions (Tasdemir & Ozkan, 2019). This situation strongly indicates that deep learning will play a critical role in promoting the accuracy of building segmentation toward practical applications of automatic mapping of features (Chen et al., 2019).

Since AlexNet overwhelmingly won the ImageNet Large-Scale Visual Recognition Challenge 2012 (LSVRC-2012) (URL-1), CNN-based algorithms have become the go-to standard in many computer vision tasks, such as image classification, object detection, and image segmentation (Wu et al., 2018a). In the beginning, researchers mainly applied patch-based CNN methods to detecting, classifying or segmenting buildings in aerial or satellite images and significantly improved the performances (Guo e al., 2016). However, as a result of extreme memory costs and low computational efficiency, Fully Convolutional Networks (FCNs) have eventually attracted more attention in this area (Wu et al., 2018a).

In this study, a comparison was made between SegNet and Fully Convolutional Networks (FCN) architectures. Inria Aerial Image Labeling Dataset which consists of 180 training images (with corresponding labels) and 180 test images was used. Two different models that use these architectures were trained using the prepared dataset and their performances have been evaluated. The creation of models and object segmentation processes were performed on the Python environment on Google Colab.

2. DATASET AND METHODOLOGY

2.1 Dataset

Dataset selected to be used is "Inria Aerial Image Labeling Dataset" (Maggiori et al., 2017). This dataset features:

- Coverage of 810 km² (405 km² for the training set and 405 km² for the testing set),
- Aerial (in color and orthorectified) imagery with a spatial resolution of 30 cm,
- Label images for two semantic classes: building and not building) (Maggiori et al., 2017).

The images from the dataset cover dissimilar urban settlements, differing from densely populated areas (e.g., Vienna) to less dense rural areas (e.g., Austrian Tyrol) (Fig 1) (Maggiori et al., 2017). The purpose of this is to improve the generalization power of the models (Maggiori et al., 2017). For example, while Chicago imagery may be used for training, the model should label images over other regions with varying conditions, urban landscape and time of the year (Maggiori et al., 2017).

Figure.1 Chicago - 5 sample image and corresponding label image (Maggiori et al., 2017)

In this study, only images from the training set were used. It is not possible to make comparisons between label images and predictions since there are no corresponding label images in the test set.

The training set contains 180 color images of size 5000×5000, covering a surface of 1500 m×1500 m each (Maggiori et al., 2017). There are 36 tiles for each of the following regions:

- Austin (TX, USA)
- Chicago (IL, USA)
- Kitsap County (WA, USA)
- Vienna (Austria)
- Western Tyrol (Austria) (Maggiori et al., 2017)

The format of the images is GeoTIFF. The pixels of label images have value 255 for building class and 0 for not building class (Maggiori et al., 2017).

To prepare the datasets for training and testing of the models, images from the training set and their corresponding label images were selected and divided into patches of size 224x224 pixels to reduce the computational cost and not lose resolution with resizing of images. Since the used architectures work with images in this size, images were prepared in size of 224x224.

To create the training dataset, 5 images and their corresponding label images were selected (Austin9, Chicago25, Kitsap18, Tyrol_w21 and Vienna15). For the test dataset, another 5 images were selected (Austin1, Chicago2, Kitsap30, Tyrol_w29 and Vienna9). During these selections, the distribution of rural and urban areas was considered. Images with no building or a low amount of buildings were removed from the datasets. Consequently, a total of 1500 images and label images for the training dataset and 300 images and label images for the test dataset were generated (Fig 2).

Figure.2 Sample image and corresponding label image from training dataset

2.2 Methodology

SegNet and FCN neural network architectures were used to train models using prepared training dataset.

2.2.1 SegNet

SegNet is a CNN architecture developed at Machine Intelligence Lab. of the University of Cambridge to design more suitable deep learning algorithms for image segmentation tasks (Badrinarayanan et al., 2017). SegNet has an encoder network and a decoder network that works according to this encoder, followed by a pixel-wise classification layer (Bozkurt, 2018).

Encoder network consists of 13 convolution layers, corresponding to the VGG16's first 13 convolution layers, which is a pre-trained network for object classification (Badrinarayanan et al., 2017). As mentioned in Badrinarayanan et al., 2017, at this network, convolutions and max-pooling are performed. At the deepest encoder output, fully connected layers are eliminated to protect higher resolution feature maps. This significantly reduces the number of parameters in the SegNet encoder network compared to other architectures.

Within the SegNet architecture, each encoder layer has its decoder layer (Badrinarayanan et al., 2017). Thus, the decoder network also has 13 layers (Badrinarayanan et al., 2017). The output of the last decoder layer produces probabilities of classes for each pixel, which feeds the classifier with probability values (Badrinarayanan et al., 2017). Illustration of the SegNet architecture is shown in Fig 3.

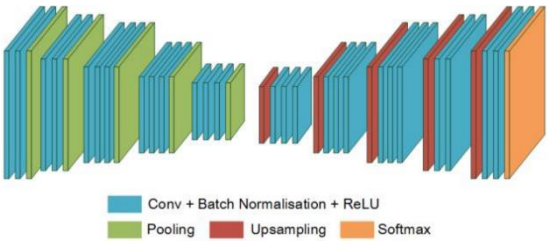

Figure.3 SegNet architecture (Du et al., 2018)

2.2.2 Fully Convolutional Networks (FCN)

Fully Convolutional Networks (FCNs) are being used for semantic segmentation of images, analysis of multi-modal medical images and classification and segmentation of high-resolution and multispectral satellite images (Long et al., 2015). In 2015, Long et al. adapted modern classification networks (AlexNet, VGGNet and GoogLeNet) into FCNs and transfer their learned representations by fine-tuning to the segmentation task. After that, they defined a novel architecture that combines semantic information from a deep, coarse layer with appearance information from a shallow, fine layer to produce accurate and detailed comprehensive (URL-2) (Fig 4).

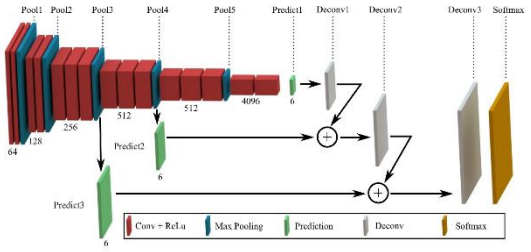

Figure.4 FCN architecture (De Souza, 2017)

FCNs built from locally connected convolutional, pooling and convolutional transpose layers (Long et al., 2015). No dense layer is used in this architecture (URL-3). The absence of dense layers makes it possible to feed the network in variable inputs (URL-3). An FCN has 2 parts:

- Downsampling path
- Upsampling path (URL-4)

As described in URL-4, downsampling path extract and interpret the context. The downsampling path consists of convolutional and max-pooling layers. Upsampling path enables precise localization of features. Upsampling path consists of convolutional, convolutional transpose and concatenate layers. Concatenation layers are used for skip connections. Skip connection is a type of connection that bypasses at least one layer. They are often used to transfer local information from the downsampling path to the upsampling path.

3. STUDY

In this study, all training and testing processes were conducted on Google Colab. Google Colab is a free Jupyter notebook environment that allows users to use free Tesla K80 GPU. It runs in the cloud and stores its notebooks and data on Google Drive.

3.1 Training and Testing

To train the models, images loaded into the network. Thereafter, training dataset split according to an 85% / 15% training/validation ratio, 1275 images and 225 images respectively.

For training, the "Adam" optimizer was used to update model parameters with a fixed learning rate of 0.001. Both models were trained for 50 iterations with a batch size of 16 using the same hyperparameters. To calculate loss values, binary cross-entropy loss function was used. Changes in training accuracy and validation accuracy over 50 iterations are shown in Fig 5.

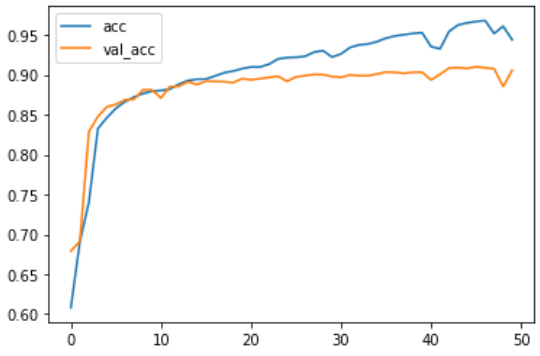

(a)

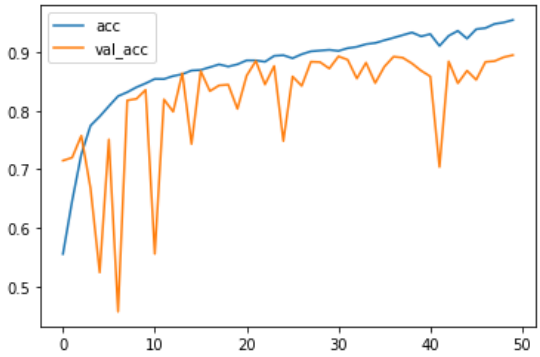

(b)

Figure.5 Accuracy values over 50 iterations (a) FCN (b) SegNet

To test the trained models, the test dataset that prepared separately from the training dataset was used.

3. RESULTS

The final accuracy results are shown in Fig 6. When the validation accuracy results examined it was seen that the model that uses FCN architecture has 94.39% training accuracy and 90.55% validation accuracy. On the other hand, the model that uses SegNet architecture has 95.49% training accuracy and 89.49% validation accuracy. FCN model is more accurate than the SegNet model by 1% according to validation accuracy results.

When training and validation accuracies of the models were compared, it was been seen that the FCN model has higher validation accuracy and the SegNet model has higher training accuracy.

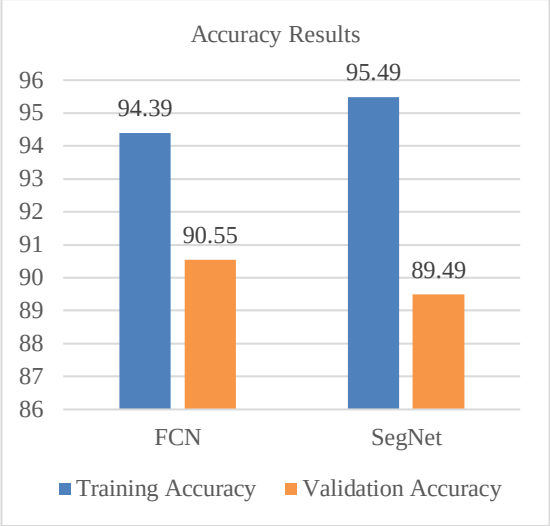

Figure.6 Training and validation accuracy results of models

When the differences between training and validation accuracies of the models examined, the model that uses SegNet architecture has a larger gap between them. This shows that the model's performance on training data is ahead of validation data. For the model that uses FCN architecture, this gap is smaller and it shows that this model is more accurate than the SegNet model.

Consequently, building segmentation was performed on the prepared test dataset using trained models. Examples from test, label and segmented images are shown in Fig 7 and 8.

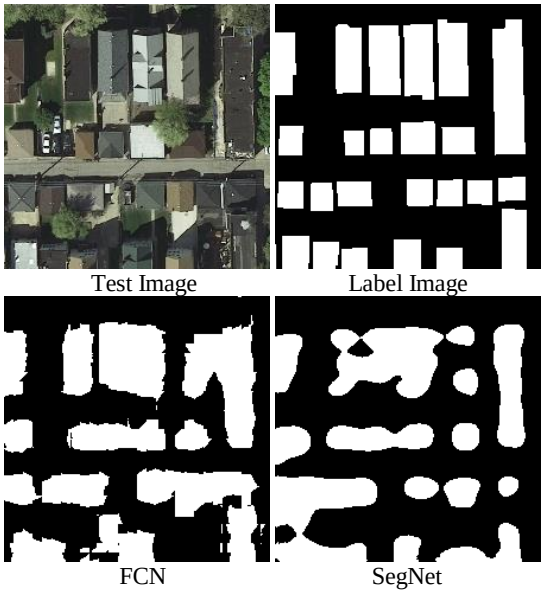

Figure.7 Segmentation results for test image 81

Figure.8 Segmentation results for test image 165

4. CONCLUSIONS

In this study, building segmentation from high-resolution images using SegNet and FCN neural network architectures were realized. Comparisons between these architectures were made. Models were trained and tested using datasets prepared from images from Inria Aerial Image Labeling Dataset.

It was observed that the model that uses FCN architecture gives more accurate results. It has higher accuracy and a smaller difference between training and validation accuracies. This can also be observed from the predicted segmentation results.

Further studies could include more datasets and different neural network architectures to make comparisons. Dataset could be augmented with unused images from Inria Dataset. More data to train the models would increase their performances. For this study, default settings were used for hyperparameters. Hyperparameter tuning could be done to improve the performances of the models. This is because hyperparameter optimization is crucial to achieve maximum performance.

REFERENCES

Akbulut, Z., Ozdemir, S., Acar, H., Dihkan, M., & Karsli, F. (2018). Automatic extraction of building boundaries from high resolution images with active contour segmentation. International Journal of Engineering and Geosciences, 3(1), 37-42.

Badrinarayanan, V., Kendall, A., & Cipolla, R. (2017). Segnet: A deep convolutional encoder-decoder architecture for image segmentation. IEEE transactions on pattern analysis and machine intelligence, 39(12), 2481-2495.

Bozkurt S. (2018). Derin Ogrenme Algoritmalari Kullanilarak Cay Alanlarının Otomatik Segmentasyonu (Master's Thesis). YTU, Istanbul.

Chen, Q., Wang, L., Wu, Y., Wu, G., Guo, Z., & Waslander, S. L. (2019). Aerial imagery for roof segmentation: A large-scale dataset towards automatic mapping of buildings. ISPRS journal of photogrammetry and remote sensing, 147, 42-55.

Comert, R., Kucuk, D., & Avdan, U. (2019). Object Based Burned Area Mapping with Random Forest Algorithm. International Journal of Engineering and Geosciences, 4(2), 78-87.

Cordts, M., Omran, M., Ramos, S., Rehfeld, T., Enzweiler, M., Benenson, R., Franke U., Roth S. & Schiele, B. (2016). The cityscapes dataset for semantic urban scene understanding. In Proceedings of the IEEE conference on computer vision and pattern recognition (pp. 3213-3223).

Deng, J., Dong, W., Socher, R., Li, L. J., Li, K., & Fei-Fei, L. (2009). Imagenet: A large-scale hierarchical image database. In 2009 IEEE conference on computer vision and pattern recognition (pp. 248-255). IEEE.

De Souza W. (2017). Semantic Segmentation using Fully Convolutional Neural Networks. Retrieved 19.03.2020, from https://medium.com/@wilburdes/semantic-segmentation-using-fully-convolutional-neural-networks-86e45336f99b

Du, Z., Yang, J., Huang, W., & Ou, C. (2018). Training SegNet for cropland classification of high resolution remote sensing images. In AGILE Conference.

Everingham, M., Van Gool, L., Williams, C. K., Winn, J., & Zisserman, A. (2010). The pascal visual object classes (voc) challenge. International journal of computer vision, 88(2), 303-338.

Guo, Z., Shao, X., Xu, Y., Miyazaki, H., Ohira, W., & Shibasaki, R. (2016). Identification of village building via Google Earth images and supervised machine learning methods. Remote Sensing, 8(4), 271.

He, K., Zhang, X., Ren, S., & Sun, J. (2016). Deep residual learning for image recognition. In Proceedings of the IEEE conference on computer vision and pattern recognition (pp. 770-778).

Krizhevsky, A., Sutskever, I., & Hinton, G. E. (2012). Imagenet classification with deep convolutional neural networks. In Advances in neural information processing systems (pp. 1097-1105).

LeCun, Y., Boser, B., Denker, J. S., Henderson, D., Howard, R. E., Hubbard, W., & Jackel, L. D. (1989). Backpropagation applied to handwritten zip code recognition. Neural computation, 1(4), 541-551.

Lin, T. Y., Maire, M., Belongie, S., Hays, J., Perona, P., Ramanan, D., Dollar P. & Zitnick, C. L. (2014). Microsoft coco: Common objects in context. In European conference on computer vision (pp. 740-755). Springer, Cham.

Long, J., Shelhamer, E., & Darrell, T. (2015). Fully convolutional networks for semantic segmentation. In

Proceedings of the IEEE conference on computer vision and pattern recognition (pp. 3431-3440).

Ma, L., Li, M., Ma, X., Cheng, L., Du, P., & Liu, Y. (2017). A review of supervised object-based land-cover image classification. ISPRS Journal of Photogrammetry and Remote Sensing, 130, 277-293.

Maggiori, E., Tarabalka, Y., Charpiat, G., & Alliez, P. (2017). Can semantic labeling methods generalize to any city? the inria aerial image labeling benchmark. In 2017 IEEE International Geoscience and Remote Sensing Symposium (IGARSS) (pp. 3226-3229). IEEE.

Sevgen, S. C. (2019). Airborne lidar data classification in complex urban area using random forest: a case study of Bergama, Turkey. International Journal of Engineering and Geosciences, 4(1), 45-51.

Tasdemir, S., & Ozkan, I. A. (2019). Ann approach for estimation of cow weight depending on photogrammetric body dimensions. International Journal of Engineering and Geosciences, 4(1), 36-44.

URL-1, 2012, http://www.image-net.org/challenges/LSVRC/2012/results.html, [26.03.2020]

URL-2, 2017, https://meetshah1995.github.io/semantic-segmentation/deep-learning/pytorch/visdom/2017/06/01/semantic-segmentation-over-the-years.html, [19.03.2020].

URL-3, 2020, https://towardsdatascience.com/implementing-a-fully-convolutional-network-fcn-in-tensorflow-2-3c46fb61de3b, [19.03.2020].

URL-4, http://www.deeplearning.net/tutorial/fcn_2D_segm.html, [19.03.2020]

Vakalopoulou, M., Karantzalos, K., Komodakis, N., & Paragios, N. (2015). Building detection in very high resolution multispectral data with deep learning features. In 2015 IEEE International Geoscience and Remote Sensing Symposium (IGARSS) (pp. 1873-1876). IEEE.

Wu, G., Guo, Z., Shi, X., Chen, Q., Xu, Y., Shibasaki, R., & Shao, X. (2018a). A boundary regulated network for accurate roof segmentation and outline extraction. Remote Sensing, 10(8), 1195.

Wu, G., Shao, X., Guo, Z., Chen, Q., Yuan, W., Shi, X., Xu Y. & Shibasaki, R. (2018b). Automatic building segmentation of aerial imagery using multi-constraint fully convolutional networks. Remote Sensing, 10(3), 407.

International Journal of Engineering and Geosciences (IJEG),
Vol; 5, Issue; 3, pp. 144-149, October, 2020, ISSN 2548-0960, Turkey,
DOI: 10.26833/ijeg.648847

RADAR CROSS SECTION ANALYSIS OF UNMANNED AERIAL VEHICLES USING PREDICS

Caner Özdemir [1,2]*

[1]Mersin University, Engineering Faculty, Department of Electrical-Electronics Engineering, Mersin, Turkey (cozdemir@mersin.edu.tr); **ORCID 0000-0003-2615-4203**
[2]Emtech Information Technologies Corporation, Mersin Technological Development Zone, Yenişehir, Mersin, Turkey (caner. ozdemir@emtechbilisim.com)

*Corresponding Author, Received: 20/11/2019, Accepted: 29/01/2020

ABSTRACT: In this study, a quantitative radar cross section (RCS) analysis of different unmanned aerial vehicle (UAV) models were accomplished by means of a series of RCS simulations. The simulations were carried out by high-frequency RCS simulation and analysis tool called PREDICS. To quantify the RCS features of the UAV model, both the angle-variation and frequency-variation simulations for all polarization excitations were performed. The results of the simulations suggested that RCS values were dramatically varying with respect to look angle with some special angles providing the large values of RCS. Generally, the RCS values of the UAV model was increasing with frequency as expected. A quantitative radar detection range analyses were also accomplished to assess the visibility of both the military-type and civil-type UAV models. The outcome of these studies has suggested that large-size UAV model can be easily detected by a high-sensitive radar on the ranges of tens of kilometers while these numbers reduce to a few kilometers for a civilian UAV model that is much smaller than the its military counterpart.

Keywords: *Radar Cross Section, Unmanned Aerial Vehicle, Radar Visibility, RCS simulation*

1. INTRODUCTION

For the last decade, the number of Unmanned Aerial Vehicles (UAVs) that are being used in numerous applications has been extensively increased due to growing demand from both the military and civil sectors (Thite *et al.*, 2012; Pieraccini *et al.*, 2017; Ananenkov, *et al.*, 2018). One of the use of UAVs is for remote sensing applications (Ulvi *et al.*, 2016; Akar, 2017, Ulvi, 2018). In a parallel manner, the need to detect such vehicles becomes really crucial for the safety on people. In military practices, UAVs are generally being used for reconnaissance, surveillance and targeted attacks (Ryapolov, *et al.*, 2014). Therefore, it becomes very vital to sense and also make them ineffective before completing their offensive missions to avoid life losses and injuries. While their military usages provide direct danger for human health and life, their civil usages may sometimes provide risky and hazardous situations like accidents. For example, UAVs can be a serious threat for the flight safety according to Aviation authorities. It is no doubt that drones and small UAVs may not be perceived by the radar of either airport's tower and/or from airplanes that are coming in or going out from the runways. Furthermore, small, civilian-type UAVs can also be used offensive purposes such as terrorist attacks. Therefore, there is a need for assessing and analyzing the radar visibility characteristics of UAVs by calculating the radar cross section (RCS) of such vehicles.

In this paper, we represent a study for calculating and analyzing the RCS values of some generic UAVs at X-band of frequencies. The RCS simulations have been carried out by our recently developed RCS simulation and analysis software called PREDICS (Özdemir *et al*, 2014a; Özdemir *et al*, 2014b). The simulations are conducted in aiming to evaluate the detectability of UAVs by radar sensors, especially at X-band. For this purpose, a quantitative analysis and assessment on the detection of UAV-type targets by a nominal radar has been made.

For this paper, two different generic UAV models are taken into account. These models are quite similar to the ones that are commonly used in both military and civil applications.

2. RCS SIMULATION OF A MILITARY-TYPE UAV MODEL: "MIL-UAV"

The computer aided design (CAD) of UAV model named as Mil-UAV that was used in PREDICS simulation can be seen in Fig.1. This model was selected because it has very similar characteristics of military UAVs that are usually significantly bigger than civil ones. The perspective view of Mil-UAV is seen Fig.1(a). The top and front view of the model are shared in Fig. 1(b). As it can be read from the figure that the wing extend of Mil-UAV is 14.73 m. The side view of Mil-UAV is plotted in Fig. 1(c). The total length and height of the model are 8.22 m and 2.40 m, respectively. During the PREDICS simulation, the material of the model is assumed to be perfect electric conductor (PEC).

RCS simulation of the Mil-UAV has been accomplished by the PREDICS simulator (Özdemir *et al*, 2014a; Özdemir *et al*, 2014b). PREDICS is a fast and effective simulation tool for the fast and accurate calculation of RCS from electrically large and complex-shaped platforms at high frequencies. The detailed information about PREDICS tool; including the theory behind the code and other technical features can be reached at (Özdemir *et al*, 2014a; Özdemir *et al*, 2014b; Kırık *et al*, 2019). The main graphical user interface (GUI) screen of PREDICS for the simulation of Mil-UAV is viewed in Fig. 2.

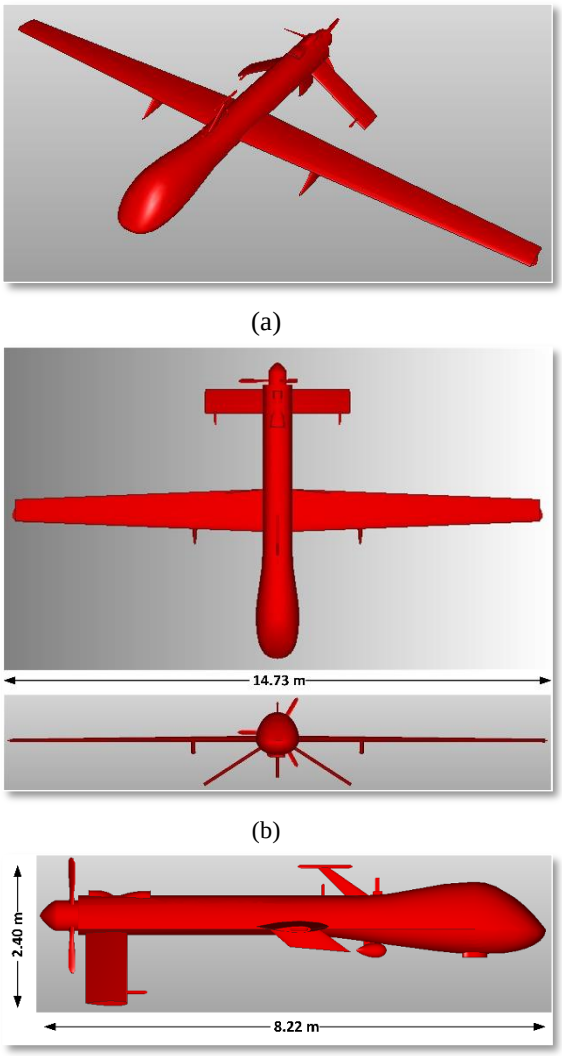

(a)

(b)

(c)

Fig. 1. Generic military UAV model: Mil-UAV (a) Perspective view, (b) Top and front view, and (c) side view

To evaluate and the RCS characteristics of Mil-UAV, two sperate RCS simulations have been carried out. Firstly, angular RCS variation for a fixed frequency has been explored. Then, the frequency RCS variation for some special look-angles that provide high scattering has also been done by the help of the RCS run. Below are the details and the outcome of these simulations.

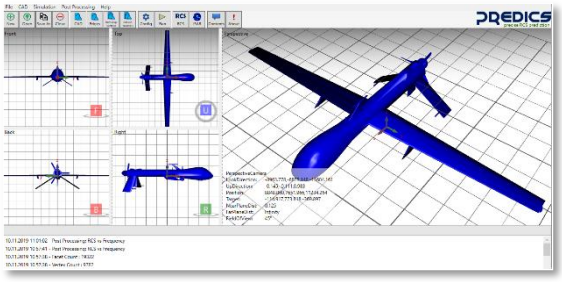

Fig. 2. PREDICS simulation screen for Mil-UAV

2.1. RCS variation over angles

In the first simulation, monostatic RCS variation for the azimuth and elevation look-angles at the fixed frequency of 10 GHz has been used. The physical optics (PO) and shooting and bouncing ray (SBR) solvers of PREDICS have been utilized. The ray density merit of 10 rays per wavelength has been used for precise RCS computation. For the PREDICS simulation, horizontal angles ranging from 0° (nose-on case) to 180° (back-side case) for a total of 121 distinct horizontal angles and vertical angles ranging from 90° (horizon case) to 111° (-21° below horizon case) for a total of 15 discrete vertical angles were included. These angles were decided based on the scenarios of radar looking towards an UAV in the air. Both co-polarization cases of vertical-vertical (VV) and horizontal-horizontal (HH) were included in the RCS simulation. In Fig.3(a) and (b), RCS map results of Mil-UAV for VV polarization are given in polar and Cartesian coordinates, respectively.

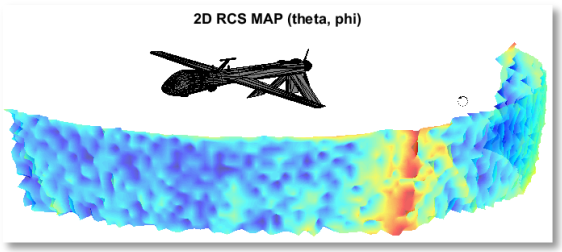

(a)

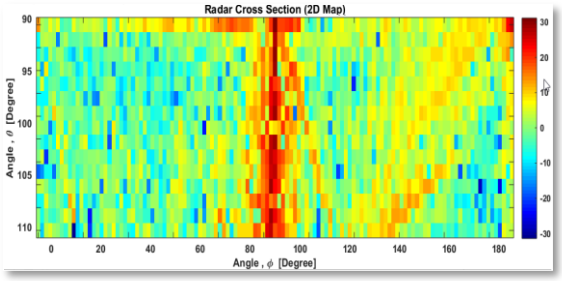

(b)

Fig. 3. 2D Angular VV-polarization RCS variation simulation result for Mil-UAV target at 10 GHz represented using RCS map plot in (a) polar coordinates, (b) Cartesian coordinates

As it can be seen from Fig.3, the highest RCS values occur at the broad-side angles around $\phi = 90°$ for almost all vertical angles. The dynamic range of the display is selected as 65 dB. To better interpret the highest RCS values, the one-dimensional (1D) horizontal RCS variation at $\theta = 90°$ for both VV and HH polarizations are plotted in Fig.4 as blue and red solid lines, respectively. One can fairly observe that the maximum value of RCS is equal to 31.18 dBsm (1,312.2 m^2) for the look angle of ($\theta = 90°, \phi = 90°$). If Fig.3 is carefully analyzed, the average RCS value can be calculated as 11.64 dBsm (10.66 m^2). Based on these calculated RCS results; therefore, a military UAV that has a similar size of a manned aircraft can produce RCS values that are not different than that of an aircraft. This result suggested that such UAVs can be easily detected by a radar from tens of kilometers away as it will be explored in Section 3.

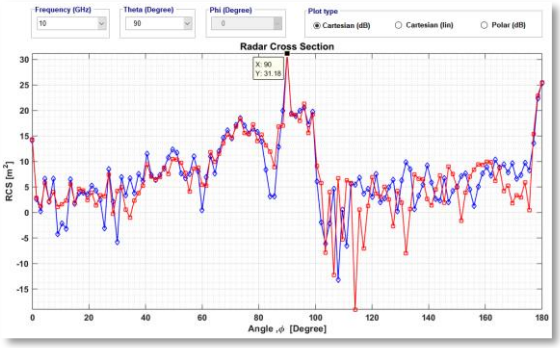

Fig. 4. 1D horizontal RCS variation simulation result for Mil-UAV at 10 GHz and $\theta = 90°$

2.2. RCS variation over frequencies

For another experiment, Mil-UAV's RCS merit for various microwave frequency values has been studied. For this purpose, the monostatic RCS variation over frequencies for the fixed look angle of ($\theta = 90°, \phi = 90°$). Again, the ray density of 10 rays per wavelength together with PREDICS's PO+SBR solver were used. The frequency was varied from 6 GHz to 18 GHz for a total of 101 discrete frequencies. The aim of this simulation was to monitor if the RCS values were increasing for the higher frequencies or not. The simulation look-angles have been chosen as the look-angles that provide the highest values of RCS outcomes that were obtained in Fig. 3 and 4. In Fig. 5, the simulated RCS results for VV and HH polarizations are shown as blue and red solid lines, respectively. As expected, the RCS values tend to increase as the frequency increases. For the selected band of frequency values from 6 GHz to 18 GHz, the maximum RCS value of 34.80 dBsm (3,019.95 m^2) was obtained for the frequency of 14.52 GHz.

3. RCS SIMULATION OF A CIVILIAN-TYPE UAV MODEL: "CIV-UAV"

The CAD model of a civilian type UAV model called as Civ-UAV that was used in PREDICS's RCS simulations is given in Fig.6. This model has characteristics that are common in many civilian UAVs. The size of this model is quite smaller than that of Mil-UAV. The perspective view of Civ-UAV is depicted Fig. 6(a). The top and front view of the model are given in Fig. 6(b). As it can be seen from the figure the wing extend of

Civ-UAV is 240 cm. The side view of Mil-UAV is also plotted in Fig. 6(c). The total length and height of the model are 120 cm and 20 cm, respectively. During the PREDICS simulation, the material of the model is taken as PEC.

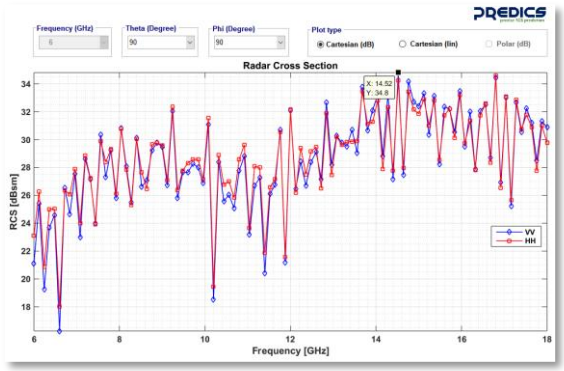

Fig. 5. Mil-UAV's RCS frequency variation for the look-angle of ($\theta = 90°, \phi = 90°$)

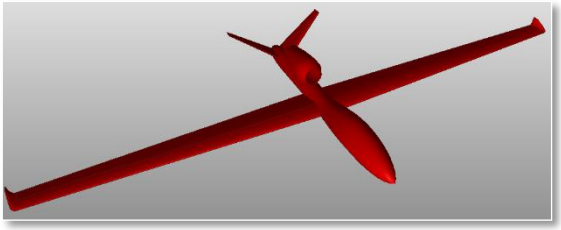

(a)

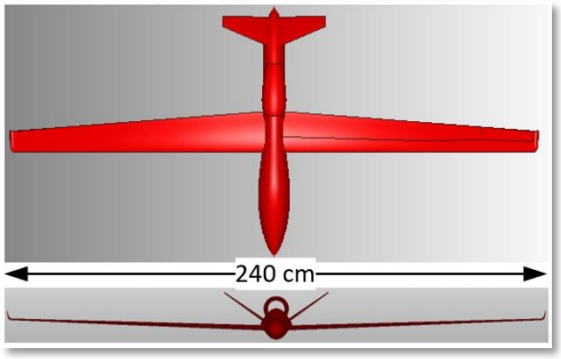

(b)

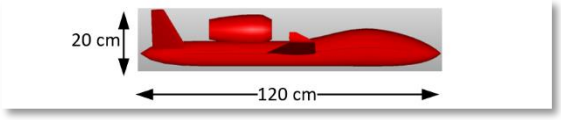

(c)

Fig. 6. Generic civilian type UAV model: Civ-UAV (a) Perspective view, (b) Top and front view, and (c) side view

PREDICS software has been used for the RCS simulation of the Civ-UAV. The RCS variation with respect to azimuth angles, elevation angles and various frequencies are given as separate studies below:

3.1. RCS variation over angles

To comprehend the RCS values of Civ-UAV model; first, angular RCS variation has been evaluated by collecting the VV- and HH-polarized monostatic RCS values for both the azimuth and the elevation angles at the fixed frequency of 10 GHz. Again, (PO+SBR) solver of PREDICS was used by taking 10 rays per wavelength for the ray-tracing and field-tracing procedures of the code. For the simulation, a total of 121 separate horizontal angles ranging from 0° (nose-on case) to 180° (back-side case) and a total of 15 different vertical angles ranging from 90° (horizon case) to 111° (-21° below horizon case) were considered similar to the simulation for Mil-UAV model. In Fig.7(a) and (b), RCS map results of Civ-UAV for VV polarization are given in polar and Cartesian coordinates, respectively. One can easily notice from this RCS map results that hot point angles are from the front (around $\phi = 0°$) and from the side (around $\phi = 90°$) from the UAV model. The simulation suggests that the RCS values are stay high around $\phi = 0°$ for almost all selected vertical angles.

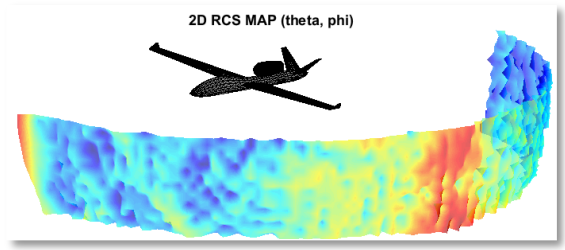

(a)

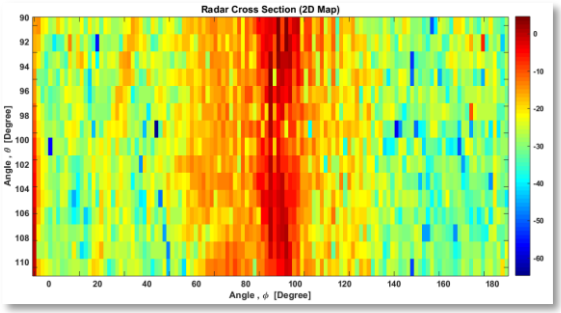

(b)

Fig. 7. 2D Angular VV-polarization RCS variation simulation result for Civ-UAV target at 10 GHz represented using RCS map plot in (a) polar coordinates, (b) Cartesian coordinates

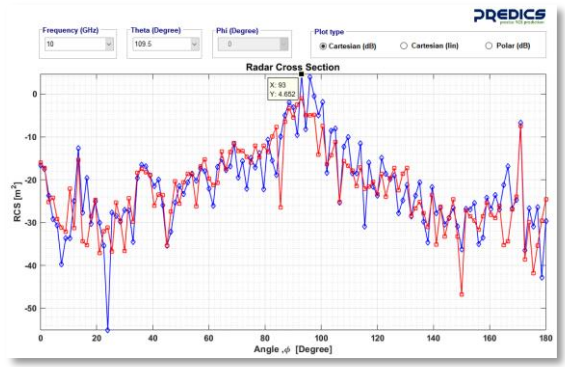

Fig. 8. Civ-UAV's RCS frequency variation for the look-angle of ($\theta = 109.5°, \phi = 93°$)

To better comprehend the uppermost RCS values, the 1D horizontal RCS variation at $\theta = 109.5°$ for both VV and HH polarizations are given in Fig. 8 as blue and red solid lines, respectively. It can be easily read from the figure that the highest RCS value is equal to 4.652 dBsm (2.92 m^2) for the look angle of ($\theta = 109.5°, \phi = 93°$). Then, the average RCS value of data in Fig. 7 has been calculated as -12.69 dBsm (0.054 m^2).

3.2. RCS variation over frequencies

In the second RCS study for the Civ-UAV model, monostatic RCS variation over frequencies ranging from 6 GHz to 18 GHz for a total of 100 discrete frequencies at the look angle of $\theta = 109.5°$ and $\phi = 93°$ has been examined. The resultant PREDICS's RCS simulation result for VV- and HH-polarizations are given in Fig. 9 as blue and red solid lines, respectively. It is observed that RCS values are somewhat fluctuating between -25 dBsm to 5 dBsm for the selected frequencies of interest. The maximum monostatic RCS value of 4.96 dBsm (3.13 m^2) occurs for HH polarization at 14.36 GHz.

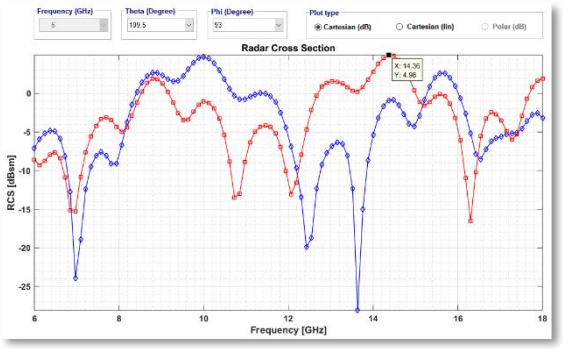

Fig. 9. Civ-UAV's RCS frequency alteration for the look-angle of ($\theta = 109.5°, \phi = 93°$)

4. RADAR DETECTABILITY STUDY FOR THE UAV MODELS

After completing RCS simulations that provided the RCS analysis studies for the selected UAV models, a radar detectability study has also been carried out to assess the detection ranges of both UAV models.

4.1 Range of radar detection

The detection range of radar; i.e., the far most distance of the target that can be spotted over the noise floor by the radar can be calculated by using the following formula (Özdemir, 2012):

$$R_{det} = \left(\frac{P_{rad}}{P_{min}} \cdot \frac{(\lambda G)^2}{(4\pi)^3} \cdot \sigma\right)^{1/4} \quad (1)$$

Here, P_{rad} represents the radiated power from the radar and P_{min} is the sensitivity of the radar or the minimum power level that the radar receiver can sense. In the above equation, λ is the wavelength that corresponds to the operation frequency of the radar, G is the gain of the radar antenna and σ is the RCS value of the target that is tried to be detected.

4.2 Detectability study of Mil-UAV model

The detection range of Mil-UAV model has been investigated by putting nominal values for the variables within the formula in Eqn. (1). This study is explored via the Table 1 by using the RCS results that was obtained by PREDICS. The following radar parameters were assumed for a highly sensitive detection radar: Two different values of radiated powers levels of 20 dB (100 W) and 24 dB (251 W) were considered. The radar was also assumed to be working in two different sensitivity levels of -95 dB and -117 dB. The gain of the radar antenna is taken as 44 dBi that is a nominal figure for a directive radar antenna.

The corresponding detection ranges for Mil-UAV model are listed in the last column of Table 1. Based on the assumed parameters and the predicted RCS values of the UAV target at 10 GHz, it can be observed from the Table 1 that the minimum detectable range is calculated as about 5.7 km for the average RCS value of 11.64 dBsm that represents the worst-case scenario. On the other hand, the best case happens when the maximum value of RCS, 31.18 dBsm is used for the parameters given in the fourth row of Table 1. For this situation, the minimum detectable range can extend up to 83 km. In summary, the detection of a UAV that has dimensions similar to Mil-UAV can be possible at the ranges from 5 to 80 km.

Table 1. Detection range of Mil-UAV model at *f=10 GHz*

σ (dBsm)	P_{rad} (dB)	P_{min} (dB)	G(dBi)	R_{det} *(m)*
31.18	20	-95	44	18,558 m
31.18	20	-117	44	65,848 m
31.18	24	-95	44	23,364 m
31.18	24	-117	44	**82,898 m**
11.64	20	-95	44	**5, 698 m**
11.64	20	-117	44	20,218 m
11.64	24	-95	44	7,173 m
11.64	24	-117	44	25,452 m

4.2 Detectability study of Civ-UAV model

A similar detectability study has been done for the Civ-UAV model that is much smaller than the its military counterpart. The same radar parameters were used as utilized in the previous study. For the calculation of the minimum detection range of Civ-UAV model, maximum RCS value of 4.652 dBsm and average RCS value of -12.69 dBsm were used in calculating the minimum detection ranges that are listed along the last column of Table 2. For the different radar parameters that are given in other columns of Table 2, the minimum detection range is varying between approximately 1.5 km and 18 km as observed from the last column of the table. Considering the UAVs' nominal cruising speed values ranging from 50 to 100 knots, range values around a few kilometers may not be adequate for some scenarios.

Table 2. Detection range of Civ-UAV model at *f=10 GHz*

σ (dBsm)	P_{rad} (dB)	P_{min} (dB)	G(dBi)	R_{det} *(m)*
4.652	20	-95	44	4,031 m
4.652	20	-117	44	14,303 m
4.652	24	-95	44	5,0751 m
4.652	24	-117	44	**18,007 m**
-12.69	20	-95	44	**1,485 m**
-12.69	20	-117	44	5,270 m
-12.69	24	-95	44	1,870 m
-12.69	24	-117	44	6,635 m

5. CONCLUSION

In this paper, we have represented a quantitative analysis of RCS from two different UAV models; namely the Mil-UAV and Civ-UAV to assess their visibility characteristics by a nominal radar. We have utilized the high-frequency RCS simulator tool of PREDICS to perform the required electromagnetic simulations to predict their RCS values at X-band. By the help of PREDICS software, the monostatic RCS simulations of the model UAVs based on various angles and frequencies have been accomplished.

It was obtained from the simulations that RCS values for the large-size model of Mil-UAV vary vastly such as 11 dBsm on average and 31 dBsm at maximum at 10 GHz. The radar detectability study for this model has provided minimum detection ranges on the order to tens of kilometers. Such values of detection figures are good enough to sense and take measures for hostile usages of similar UAVs. On the other hand, a civilian model of Civ-UAV has yielded RCS values such as -12.67 dBsm on average and 4.652 dBsm at maximum. After completing a similar study as in the case of a Mil-UAV model, it is calculated that the minimum radar detection range extends from 1.5 km to a few kilometers. These range values may not be good enough for a radar to detect and take necessary measures to secure the targeted area of a hostile UAV.

ACKNOWLEDGEMENTS

This work was supported by Mersin University Scientific Research Unit under Project No. 2015-TP3-1160.

REFERENCES

Akar, A. (2017). Evaluation Of Accuracy of Dems Obtained From UAV-Point Clouds for Different Topographical Areas. *International Journal of Engineering and Geosciences*, 2 (3), 110-117.

Ananenkov, A. E., Marin, D. V., Nuzhdin, V. M., Rastorguev V. V., and Sokolov, P. V. (2018) "Possibilities to Observe Small-Size UAVs in the Prospective Airfield Radar," *2018 20th International Conference on Transparent Optical Networks (ICTON)*, Bucharest, 2018, pp. 1-6.

Özdemir C., Inverse Synthetic Aperture Radar Imaging with MATLAB Algorithms (2012), John Wiley & Sons, March 2012, Hoboken, New Jersey, ISBN: 978-0-470-28484-1.

Özdemir, C., Yılmaz, B., and Kırık, Ö. (2014a), "PREDICS: A new GO-PO based ray launching simulator for the calculation of electromagnetic scattering and RCS from electrically large and complex structures," *Turkish Journal of Electrical Engineering & Computer Sciences*, Vol. 22, 1255 – 1269

Özdemir, C., Yılmaz, B., Kırık, Ö., Sütcüoğlu, Ö. (2014b), "A Fast and Efficient RCS Calculation and ISAR Image Formation Tool: PREDICS", *10th European Conference on Synthetic Aperture Radar* (EUSAR 2014), Berlin.

Pieraccini, M., Miccinesi, L. and Rojhani, N. (2017) "RCS measurements and ISAR images of small UAVs," in *IEEE Aerospace and Electronic Systems Magazine*, vol. 32, no. 9, pp. 28-32, September 2017.

Ryapolov, I., Sukharevsky O., and Vasilets, V. (2014) "Radar cross-section calculation for unmanned aerial vehicle," *2014 International Conference on Mathematical Methods in Electromagnetic Theory*, Dnipropetrovsk, pp. 258-261.

Ulvi, A. Toprak, A. (2016). "Investigation Of Three-Dimensional Modelling Availability Taken Photograph Of The Unmanned Aerial Vehicle; Sample Of Kanlidivane Church.", *International Journal of Engineering and Geosciences*, 1 (1), pp. 1-7.

Ulvi, A. (2018). "Analysis of The Utility of the Unmanned Aerial Vehicle (UAV) in Volume Calculation by Using Photogrammetric Techniques." *International Journal of Engineering and Geosciences*, 3 (2), pp. 43-49.

International Journal of Engineering and Geosciences (IJEG),
Vol; 5, Issue; 3, pp. 150-159, October, 2020, ISSN 2548-0960, Turkey,
DOI: 10.26833/ijeg.649961

ANECHOIC CHAMBER MEASUREMENTS FOR CIRCULAR ISAR IMAGING AT MERSIN UNIVERSITY'S MEATRC LAB

Sevket Demirci [1]*, Caner Ozdemir [1]

[1]Mersin University, Engineering Faculty, Department of Electrical and Electronics Engineering, Mersin, Turkey
(sdemirci/cozdemir@mersin.edu.tr); **ORCID 0000-0002-3020-7067, ORCID 0000-0003-2615-4203**

*Corresponding Author, Received: 22/11/2019, Accepted: 29/01/2020

ABSTRACT: Inverse synthetic aperture radar (ISAR) imaging is a reliable detection and classification technique for maneuvering targets at near and far-field ranges. In this study, we examine the near-field circular (turntable) ISAR imaging by conducting various real measurement experiments that were performed in the microwave anechoic chamber of the Mersin University's MEATRC laboratory. The backscattered data were collected via a vector network analyzer that works as a Stepped Frequency Continuous Wave (SFCW) radar and for a number of simple and complex metal objects. The collected raw data were calibrated by using the backscattering data of a canonical object and then focused by applying a near-field backprojection image reconstruction algorithm. The resultant circular ISAR images demonstrate successful and well localized detection of various types of targets even though they are camouflaged by clothing. The obtained results reveal the preliminary efficacy of C band ISAR imaging in concealed object detection problem encountered at security checkpoints such as airports.

Keywords: *ISAR imaging, Near-field ISAR, Anechoic chamber, Concealed object detection*

1. INTRODUCTION

Inverse Synthetic Aperture Radar (ISAR) is a microwave remote sensing tool that uses target motion for the generation of an image of that target (Ozdemir, 2012). Aircrafts, helicopters, drones, ships and vehicles are amongst the common targets of ISAR imaging. In its basic mode, a two-dimensional (2D) ISAR image represents the estimate of the projection of the target's spatial reflectivity on a plane. Usually, this reflectivity map is largely dominated by contributions from some main components, termed as scattering centers. ISAR imagery has a prominent aspect in successfully exhibiting these hot points which have a critical role in target recognition (Ozdemir, 2012).

An important parameter in this context is the radar cross section (RCS) which determines the detectability metric of a target to a radar (Currie, 1989, Mensa, 1991 and Knott, 2006). A larger RCS indicates that the target can be more easily detected. Another important parameter is the resolution which defines the ability of radar to differentiate between the scattering centers. Range resolution is achieved by varying the frequency of the transmitted pulse, thus it depends on the frequency bandwidth. Cross-range resolution is obtained by varying the aspect of the target (i.e. changing the relative platform-target distance), therefore it depends on the angular data collection span. Obviously, wide angular spans improve cross-range resolution (Wehner, 1994).

Circular (or turntable) ISAR is a subcategory of ISAR which offers an effective way of utilizing the abovementioned parameters, i.e. RCS and resolution (Chen, *et al* 1980 and Kempf, *et al* 2007). To clarify, first note that circular ISAR incorporates the circular movement of a target, providing an observation coverage up to 360°. Hence, higher resolution imagery than that of narrow-angle ISAR is usually attained (Soumekh, 1999). Second, it can characterize anisotropic reflectivity mechanisms of the whole target, again due to its wide-angle feature. Therefore, it is a well-suited research and validation tool for investigating targets' scattering behaviors.

Owing to these distinct features, circular ISAR has been widely deployed in numerous tasks. For instance, in RCS prediction and imaging of military targets, the measurements are often made in RCS chamber rooms or outdoor environment by placing targets on a rotating turntable. The obtained images are then examined for the purpose of lowering the overall RCS of targets via identifying and modifying the target structure to reduce the scattered energy in a given direction (Baird, *et al* 2005, Kempf, *et al* 2007 and To, *et al* 2009). In nondestructive testing, like assessment of the deterioration of concrete structures, circular ISAR is mostly exploited to achieve high resolution maps of the material defects (Hong, *et al* 2000). In security applications such as imaging of concealed objects (Detlefsen, *et al* 2005, Bertl, *et al* 2007, Bertl, *et al* 2008, Bertl, *et al* 2010 and Sheen, *et al* 2010), a circular SAR or ISAR scanning is frequently used to obtain different views of the human body as well as in biomedical applications such as detection of tumors (Naseri, 2015, Avsar, *et al* 2016, Bicer, *et al* 2018 and Celik, *et al* 2019).

Besides its aforementioned advantages, circular ISAR has some challenges that need to be addressed for a successful application. For instance, the data collection geometry inherently presents a near-field inverse scattering problem which implies the requirement of a complex image reconstruction algorithm. Furthermore, the data collection and calibration processes should be accurately performed to benefit from circular ISAR's full potential as being very sensitive to errors.

In this paper, we aim to characterize various attributes of 2D circular ISAR imaging through microwave anechoic chamber data. Our focus is towards the S to Ku band imaging of various metal objects in order to provide a research resource for the concealed object detection problem. In our previous studies (Cetinkaya, *et al* 2011, Demirci, *et al* 2011, Demirci, *et al* 2012 and Demirci, *et al* 2013), this problem was approached by using millimeter wave band data. Herein, we evaluate the effectiveness of low frequency (up to 22 GHz) usage in penetrating through clothing camouflage. For this purpose, a series of experiments were conducted within the anechoic chamber room of the Advanced Technologies Research Center (MEATRC) laboratory at Mersin University. The calibrated images of the targets are reconstructed via near-field backprojection algorithm and analyzed in terms of resolution, far-field RCS, scattering features, frequency/angle sampling and effects of clothing obscure. The findings of these analyses and detailed discussions will be presented.

2. THEORY FOR CIRCULAR ISAR IMAGING

It is first worth noting that there are two key elements of a 2D radar reflection measurement geometry, i.e. range and cross-range. Range is the distance along the axis in the direction of the propagation of the beam whereas cross-range (or azimuth) is defined orthogonal to the range direction. As stated previously, frequency and angular diversities determine the resolutions in range and cross-range directions, respectively.

Circular ISAR takes into account the circular movement of either target or antenna to collect target's reflection information at different angular views. This can be achieved by moving the antenna on a target-centered circle or by rotating the target. Fig. 1 shows the 2D imaging geometry for the former case. The transceiver antenna transmits and receives radar waveforms, step by step, at the uniform samples of the azimuth angle positions $\emptyset$. As the look direction changes, the different geometrical information about the target can be acquired.

For such wide-angle data collections, plane-wave illumination of the whole target is usually not satisfied. The image reconstruction algorithms, therefore, should consider wavefront curvature effects to obtain focused imagery. One possible option could be the sub-aperture method which assumes planar wavefronts in smaller sub-apertures, thereby having a drawback of resolution degradation (Ozdemir, *et al* 2009). Another option could be the use of the backprojection algorithm (Munson, *et al* 1983 and Knaell *et al* 1995) which we have employed within this study. In the following, we briefly describe the formulation of this algorithm for a near-field data collection geometry.

With regard to the Fig. 1, let the target to be imaged is represented by a reflectivity function $g(x, y)$ and is assumed to be in the near-field of the antenna. The instantaneous look-angle $\emptyset$ is defined by the unit vector $\vec{u}$ which points from the origin towards the antenna. At each viewpoint, radar measures the range profile $d_{\emptyset}(r)$

given by

$$d_{\emptyset}(r) = \int_{-\infty}^{\infty}\int_{-\infty}^{\infty} g(x,y)\delta(r_u - r)dxdy \quad (1)$$

where r_u stands for the near-field range from a viewpoint to any location (x, y). Eqn. (1) is also known as *Radon Transform* of the scene which represents a projection of a three-dimensional (3D) target onto a one-dimensional (1D) function. ISAR systems generally acquire Fourier Transform (FT) data of this range profile which is expressed as

$$D_{\emptyset}(k_r) = \int_{-\infty}^{\infty} d_{\emptyset}(r)exp(-jk_r r)dr \quad (2)$$

where k_r is the wavenumber defined as $k_r = 4\pi f/c$, f is the frequency and c is the speed of light in vacuum. Stepped-frequency continuous wave (SFCW) radars measure the samples of this FT data at discrete frequency steps within a bandwidth B;

Backprojection algorithm benefits from the projection-slice theorem (Munson, *et al* 1983), whereby the measured $\boldsymbol{D_{\emptyset}(k_r)}$ can be linked to the target's FT $\boldsymbol{G(k_x, k_y)}$ via $\boldsymbol{D_{\emptyset}(k_r) = G_{\emptyset}(k_r)}$. Hence, a sampled representation of $\boldsymbol{G(k_x, k_y)}$ can be obtained from the projections $\boldsymbol{d_{\emptyset}(r)}$ measured at various observation angles. The algorithm uses this fact when utilizing the FT relationship between $\boldsymbol{g(x,y)}$ and $\boldsymbol{G(k_x, k_y)}$. Then, the resulted equation for an estimate of $\boldsymbol{g(x,y)}$ is found as

$$g(x,y) = \int_{-\pi}^{\pi}\left[\int_0^{\infty} D_{\emptyset_u}(k_r)exp(jk_r r_u)\, k_r dk_r\right] d\emptyset_u \quad (3)$$

where the bracketed term in Eqn. (3) is the 1D filtered backprojection at the angle $\emptyset_u$. Denoting this by $q_{\emptyset_u}(r_u)$, it can be simply calculated by weighting the FT of the range profile $D_{\emptyset_u}(k_r)$ with a high-frequency filter (k_r), and then by taking the 1D inverse Fourier transform (IFT). The consequential projections for different azimuth angles are then added to reconstruct an image of $g(x,y)$. In the implementation, a 1D interpolation procedure is required in image domain when the value of $q_{\emptyset_u}(r_u)$ is obtained for each pixel. At this back-projection step, if the true vector magnitudes of the near-field ranges r_u are taken, then the algorithm compensates the wavefront curvature effects. The reader is referred to (Demirci, et al, 2012) for a detailed formulation of this image reconstruction procedure.

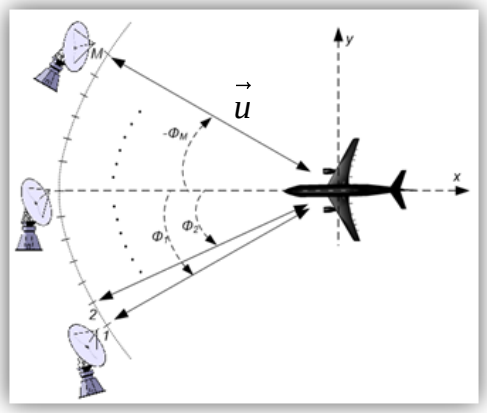

Figure.1 The geometry for 2D circular ISAR imaging (Ozdemir, 2012).

2.1 Sampling Constraints

Since the backscattering data from a SFCW radar are acquired through sampling of frequency f and azimuth angle $\emptyset$, the characteristics of the resulting image are limited by these parameters. To avoid aliasing, the sampling intervals along each dimension should satisfy the Nyquist sampling criterion. These requirements for a circular ISAR scanning become as the followings:

$$\Delta \boldsymbol{f} \leq \frac{\boldsymbol{c}}{\boldsymbol{2R_{max}}} \quad (4)$$

and

$$\Delta \emptyset \leq \frac{\boldsymbol{\lambda_{min}}}{\boldsymbol{4\rho_{max}}} \quad (5)$$

where $\Delta \boldsymbol{f}$ is the frequency step, $\Delta\emptyset$ is the angular step, $\boldsymbol{\lambda_{min}}$ is the minimum transmitted wavelength, $\boldsymbol{R_{max}}$ is the maximum unambigious range and $\boldsymbol{\rho_{max}}$ is the target's maximum distance in radial direction.

2.2 Resolutions

Spatial resolutions in ISAR images depend on the frequency bandwidth, center frequency, extent of the angular view, as well as targets' scattering characteristics. In narrow-angle case, the range and cross-range resolutions are defined according to a separable 2D coordinate system. In wide-angle case, these resolutions, however, become no longer independent and the traditional formulas cannot be readily applied. Finding an analytical solution is also known to be a difficult task for this situation. Consequently, the resolutions of wide-angle collections are usually computed via approximate methods. Herein, we adopted a method that is based on measurement of the 2D image area occupied the mainlobe return from a point scatterer. The method can be implemented with the following steps:

i. Obtain ISAR image of a point-like scatterer for a given $(\boldsymbol{f}, \emptyset)$ data set.
ii. Extract and display $\boldsymbol{-4}$ dB contour plot through the peak of target data.

iii. Calculate $-\mathbf{4}$ dB resolutions in range and cross-range as the distances between the points where the peak value has fallen by **4** dB.

The obtained values can then be used for evaluating the resolution performance of wide-angle ISAR data collection and image reconstruction procedure.

3. OPERATION PRINCIPLES OF THE EXPERIMENTS

3.1 Experimental System

Fig. 2 shows the schematic diagram of our experimental system used for reflection measurements within an anechoic chamber. It involves a vector network analyzer (VNA) with a SFCW operation, a transmitter (TX) and a receiver (RX) horn antenna in a quasi-monostatic mode and a turntable. Quasi-monostatic means antennas are co-located with a slight separation between them. The target to be observed is placed on a Styrofoam support on the top of the turntable, at a range distance R_0 away from the midpoint of the antennas. The centers of antennas and the target are all located at the same height above the ground level with zero incidence angle. The turntable angle $\emptyset$ can be varied from 0° to 360° with a resolution of $\Delta\emptyset = 0.1°$. At each angle, the turntable is stopped and the scattering response at that angle is collected by VNA for a selected frequency bandwidth. The process is then repeated for different angles by rotating the turntable to the next angular position. A control computer with a customized MATLAB program communicates with VNA and position controller to control the rotation angle, measurement trigger and data logging. Thus, the automated measurements at multiple observation angles could be achieved at high sensitivity.

3.2 Calibration Method

Data calibration plays a crucial role in research and validation to minimize the undesired echoes. In this study, we have employed background subtraction procedure to calibrate the frequency domain backscatter data captured by a SFCW radar. In this procedure, two measurements are first performed with reference to the set-up in Fig. 2. One is for the actual target and the other one is for the canonical target that are both located at the center of the turntable with a normal incidence alignment. Later, a target-free measurement for the chamber room and support materials is performed. Using the theoretical backscattering data from a canonical target, the calibrated data can then be obtained as

$$E_S(f) = \frac{E_S^{tar}(f) - E_S^{bkg}(f)}{E_S^{cal}(f) - E_S^{bkg}(f)} E_S^{cal,theo}(f) \quad (6)$$

where E_S^{tar} denotes the target's raw data to be calibrated, E_S^{bkg} denotes the measured backscatter from chamber room without the target, E_S^{cal} and $E_S^{cal,theo}$ denote, respectively, the theoretical and measured backscatter from a canonical (i.e. reference) target and $E_S(f)$ denotes the calibrated data. It must be noted that, prior to the measurements, VNA is also internally calibrated at the ends of the cables by means of a 2-port response and isolation measurements.

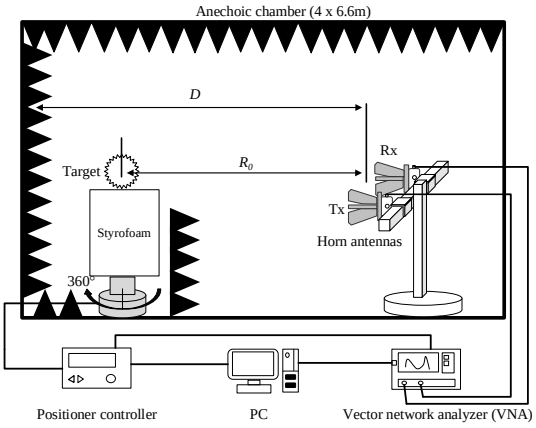

Figure.2 Illustration for the working principle of circular ISAR experiments.

4. EXPERIMENTAL RESULTS

4.1 Reflectivity of chamber walls

Before performing the imaging experiments, we first evaluated the performance of our anechoic chamber. A simple procedure explained in (Cottard, *et al* 2006) was utilized to obtain the reflectivity of the radar absorbing material that was used on the walls of the chamber. Using the geometry in Fig. 2 and locating a reference target, namely a metal plate with a size of $(a \times b) = (0.23\,m \times 0.17\,m)$ on the Styrofoam box, backscattered data were collected for frequencies ranging from 4.5 GHz to 8.5 GHz. The plate was placed perpendicular to the radar beam and precisely aligned pointing towards the mid-point of the line segment between the TX and RX antenna, laying at a distance of $R_0 = 2.64\,m$ from this point. Afterwards, a similar measurement was carried out for the absorber at a stand-off distance of $D = 2.2\,m$. The measured reflectivity level was then computed via (Cottard, *et al* 2006).

$$\boldsymbol{\sigma_0^{absorb}} = \left(\frac{\mathbf{1}}{\boldsymbol{\pi R^2}}\right) \boldsymbol{\sigma^{ref}} \left|\frac{\boldsymbol{E_s^{absorb}}}{\boldsymbol{E_s^{ref}}}\right|^2 \left(\frac{\boldsymbol{D}}{\boldsymbol{R}}\right)^4 \quad (7)$$

where $\boldsymbol{\sigma_0^{absorb}}$ is the reflectivity (i.e., normalized RCS) of the absorber, $\boldsymbol{\sigma^{ref} = 4\pi a^2 b^2 / \lambda_c^2}$ is the RCS of the metal plate with $\boldsymbol{\lambda_c}$ being the center wavelength and $\boldsymbol{E_s^{absorb}}$ and $\boldsymbol{E_s^{ref}}$ are the frequency domain data measured for the absorber and reference targets, respectively. Fig. 3(a) shows the measured range profiles obtained by taking 1D IFT of the frequency-domain data. As seen from the target's plot, the metal plate is detected at the correct range. Fig. 3(b) shows the measured reflectivity in dB, plotted as a function of frequency. It is seen that the reflectivity level varies between $-\mathbf{40}$ dB and $-\mathbf{70}$ dB indicating an acceptable absorber characteristic.

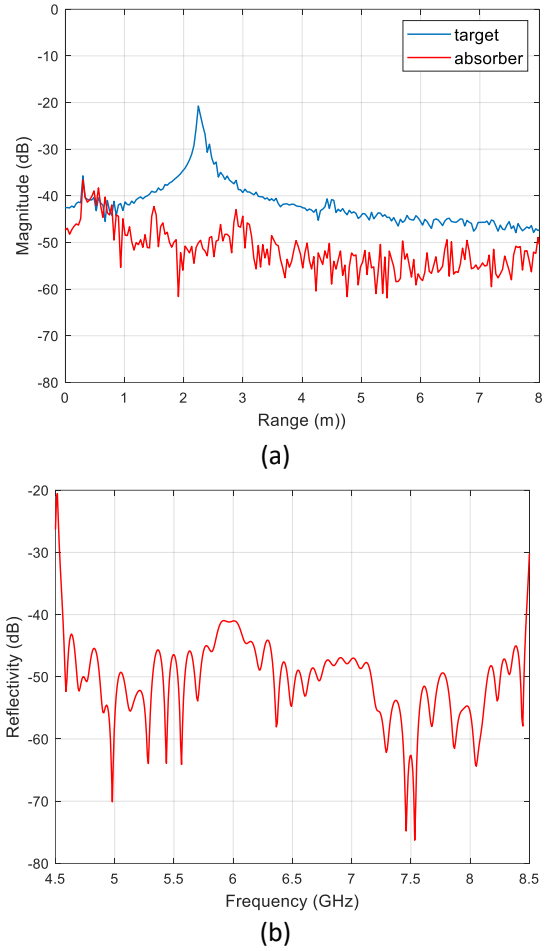

Figure.3 Results for chamber wall measurements with a plate reference target: (a) range profiles, (b) reflectivity of the absorber.

4.2 Imaging experiments

The experiments were intended to determine whether circular ISAR imaging at low frequencies (i.e. up to 22 GHz) has a possible application in monitoring concealed objects. For this purpose, various metallic objects either naked or hidden under clothing were selected as targets. The measurements were conducted within the anechoic chamber room ($4m \times 6.6\,m$) at the Mersin University's MEATRC laboratory.

A total of five consecutive experiments were performed in the quasi-monostatic arrangement of rectangular double-ridged horn antennas (Geozondas GZ0126DRH, $1-26$ GHz) that were spatially separated by a distance of $300\,mm$ apart. In all experiments, except the fourth one, the frequency of VNA was altered from 4.5 GHz to 8.5 GHz sampling a total of 501 points. In the fourth experiment, however, two dataset were acquired at 801 frequency points within the two frequency ranges; i.e. 1 GHz to 11 GHz and 11 GHz to 22 GHz. Two VNAs were used to cover these frequencies; one is Agilent E5071B (300 kHz to 8.5 GHz) and the other is handheld Keysight (Agilent) Fieldfox N9918A ((30 kHz to 26.5 GHz)). In all cases, backscatter data were collected by rotating the target under test from 0 to 360° with 1° increments and with an antenna to target distance of $R_0 = 2.18\,m$. It is worth remarking that sampling requirements given in Eqn. (4) and Eqn. (5) were met with the chosen angular and frequency intervals, assuming a maximum target size of around 40 cm.

The data processing steps that we applied prior to imaging are as follows: First, a temporal smoothing function, i.e., Hanning window was applied to the frequency-domain data for sidelobe control. A 1D IFT was then performed to convert the frequency-domain data into time-domain. Next, a time gating was applied to filter out the unwanted echoes falling outside the target region. The resulted signals were then converted again into frequency-domain and calibrated by using Eqn. (6) with the measurement data of background and a conducting sphere with a diameter of 5 cm. Finally, the reflectivity images were reconstructed by a near-field backprojection imaging algorithm. The obtained images and the relevant results are presented in the following.

4.2.1 Experiment 1: Two cylinders

For the first experiment, we have selected two small metal (made of cupper) cylinders that have diameters of 2 cm and lengths of 15 cm as seen in Fig. 4. After processing the raw data through the processes explained in the previous section, the 2D reflectivity image has been reconstructed by the help of backprojection imaging algorithm, as depicted in Fig. 5(a). The displayed dynamic range is 40 dB. The image shows that each cylinder is well-focused at its true location around wherein the majority of the backscattered energy is confined. Thus, the image features shows an approximate point type scattering, as expected owing to the fact that the cylinders have diameters in the order of wavelength. However, the responses also include ring-shaped defocusing signatures centered at the cylinders' exact locations. These can be well attributed to the layover phenomenon as encountered in 2D imaging of a 3D target under wide azimuthal viewing (Demirci, et al 2015). Moreover, the scattering interactions can also be noticed from the low-level returns located between the two cylinders.

Fig. 5(b) shows the frequency average RCS values of as a function of azimuth angle. The plot has been obtained by first calculating the magnitude squared values of the calibrated frequency-domain data measured at each angle and then averaging the result over the examined frequency band. The presented plot in Fig. 5(b) corresponds to the frequency band of 4.5 GHz to 8.5 GHz. The measured RCS values demonstrate a fluctuation within -4 dB and -12 dB, indicating a high reflection energy over the entire angular views. This is due to isotropic scattering mechanism of cylinder-like targets.

To measure the spatial resolutions, contour plots through the peak of the upper cylinder has been retrieved from the image and sketched as shown in Fig. 5(c). The outer contour corresponds to the -4 dB, and thus its extent in range and cross-range dimensions gives the -4 dB resolutions in the respective direction. The distances were found to be same and equal to about 1 cm. This good resolution was expected because of the high-resolution capability of full-aperture angular scanning.

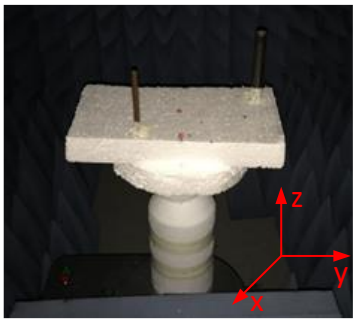

Figure 4. Photograph of the target used in Experiment 1.

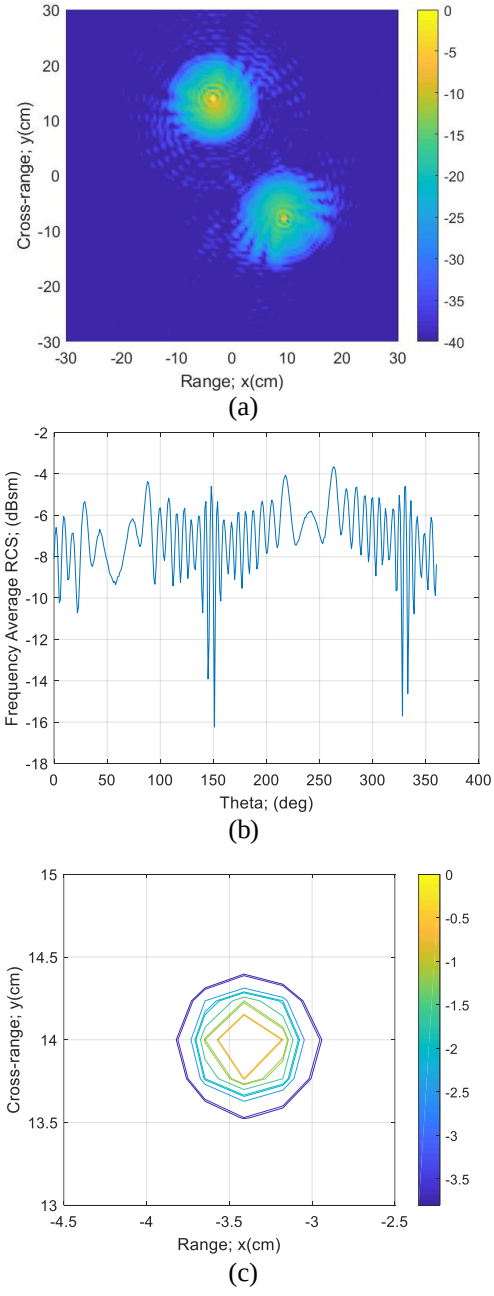

Figure 5. Results for Experiment 1: (a) Circular ISAR image, (b) frequency average RCS, (c) contour plots around the peak value.

4.2.2 Experiment 2: Four plates

Fig. 6 shows the photograph of the target used in the second experiment. The target consisted of four metal plates, placed vertically with respect to the line of sight (LOS) of the radar. The plates on the right and left have larger lengths and widths than the other ones. Fig. 7(a) shows the reconstructed image displayed within the dynamic range of 30 dB. All four plates can be readily identified through their high intensity image signatures. However, the signatures are seen, again, to have layover artifacts shown up vertical lines in this case. The relative sizes of the plates can also be deduced by considering the spatial extent of these signatures. More clearly, the plates shown on the top and bottom of the figure are larger in size, thus they produce wider strong responses.

RCS pattern as the objects is rotated about its vertical axis is shown in Fig. 7(b). It is well known that, RCS of a plate makes a peak when the radar's LOS vector is perpendicular to the plate's surface. When the incident angle deviates from this direction, RCS value decreases, because of the scattering of the wave in different directions other than the direction of the receiving antenna. The plot manifests this fact by exhibiting high RCS values at 0° and 180° views.

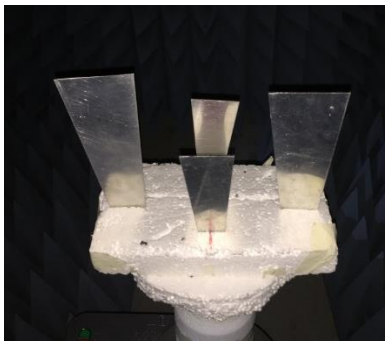

Figure 6. Photograph of the target used in Experiment 2.

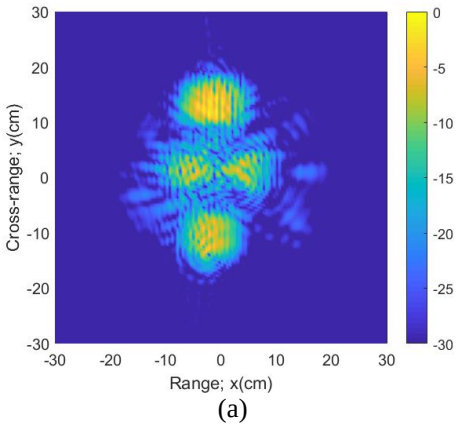

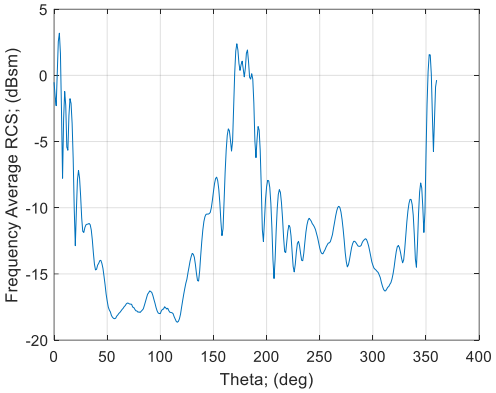

(b)

Figure 7. Results for Experiment 2: (a) Circular ISAR image, (b) frequency average RCS.

4.2.3 Experiment 3: A screw wrench

As a third experiment, a more complex object that is a screw wrench with a length of 36 *cm* was chosen. Photographs of the target can be seen from Fig. 8, of which the one on the left shows the target's alignment during the experiment. The generated image for this aspect is given in Fig. 9(a). The quality of the image is quite satisfactory, revealing the true size of the target in cross-range direction. However, the size in range direction is not correctly mapped since the energy in this direction is seen to be spread out over a larger region. This may be resulted from the lateral alignment of the target that gives rise to low RCS values. Despite this, some strong scattering centers are shown to be focused at the front and rear parts of the object.

RCS pattern shown in Fig. 9(b) has similar characteristic with those observed for the metal plates, which are both having maximum values at 0° and180°. For the current case, the two sides of the wrench faces directly to the radar at these views, thereby giving rise to high backscattered power, as one would expect. The complex structure of the front part, however, is also seen to produce relatively high RCS value at 90°.

Figure 8. Photograph of the target used in Experiment 3.

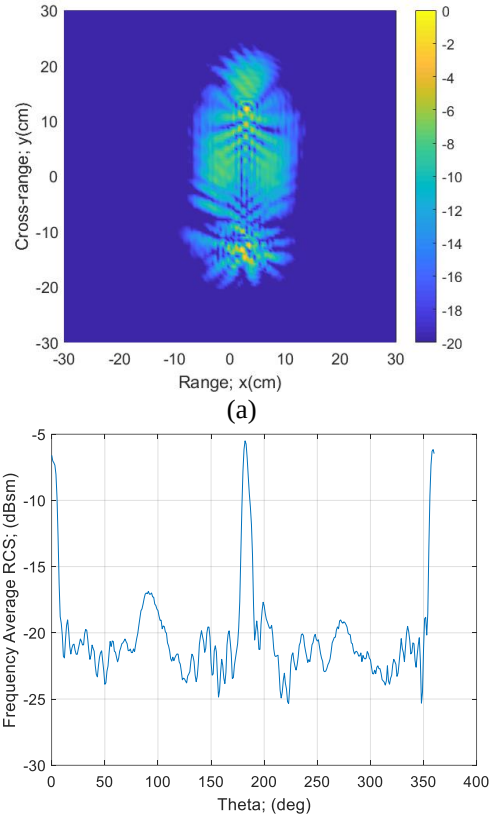

(a)

(b)

Figure 9. Results for Experiment 3: (a) Circular ISAR image, (b) frequency average RCS.

4.2.4 Experiment 4: A handgun

As for the fourth experiment, backscattering data from a real handgun were gathered within the two different frequency ranges, namely, 1 GHz to 11 GHz and 11 GHz to 22 GHz, with intended purpose of investigating the effect of frequency dependence on image signatures. The resulted images are provided in Fig. 9. At first glance, it is noticed that each image successfully displays the target's outline within the 20 dB dynamic range. Also, the strong returns are seen to come from the gun's magazine, hammer (rear), trigger/trigger guard and muzzle (front) parts in both case. However, the higher-frequency result has shown an overall improvement in image resolution than that of lower-frequency. This improvement is in good agreement with the Eqn. (5) which implies that the use of higher frequencies improves cross-range resolution for a fixed frequency bandwidth. The gun's several parts are more clearly delineated in the image for $11-22$ GHz frequency bandwidth, indicating better visualization and identification capability. This advance may be of particular significance in detecting small, concealed objects.

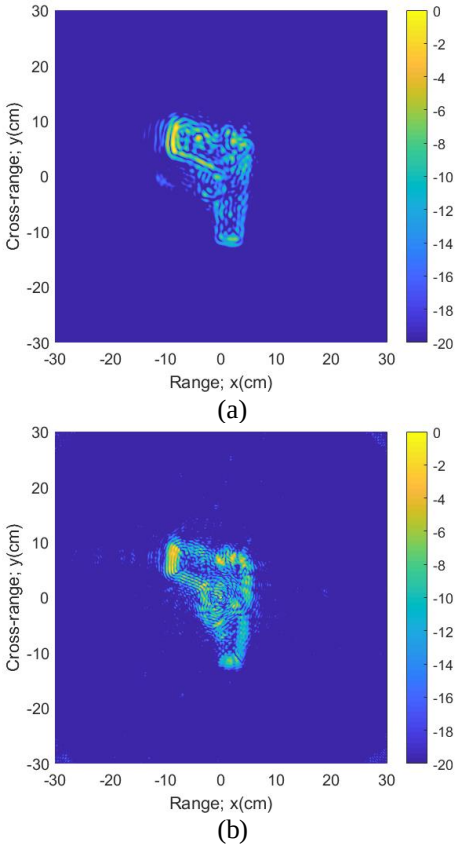

Figure 10. Circular ISAR images for Experiment 4: (a) $1-11$ GHz, (b) $11-22$ GHz frequency range.

4.2.5 Experiment 5: A handgun with clothing covering

It is well known that millimeter waves (e.g., 30 GHz to 300 GHz) are capable of penetrating clothing thereby detecting small objects under clothing thanks to their small wavelengths (Demirci, et al, 2012). In this experiment, we aimed to provide an initial result for determining to what extent the C-band frequencies could reveal the image of a relatively large target hidden under clothing. For this purpose, the same handgun used in the previous experiment, was scanned in its two different conditions; i.e., one with no cover and the other was covered with a jacket. Note that the bandwidth employed in the experiment was 4 GHz ranging from 4.5 GHz to 8.5 GHz and the standoff distance was 2.18 m, as stated before.

The reconstructed full-aperture ISAR images are shown in Fig. 11. The outline of the handgun can be discerned from both images, though it is less clearly displayed for the covering case. In each situation, the strong scatterers are shown to be located, again, at the gun's magazine, hammer and muzzle parts. As seen from Fig. 11(b) clothing covering presents a distribution of some cluttering (unwanted) echoes positioned around the target region, thus masking target signatures. Nevertheless, it can be stated that that such artifacts, as having relatively low RCS values, do not strongly influence detection performance, since the current target has strong ISAR scattering features that reflect the shape of the target. However, it may not be always possible to overcome this difficulty, if a small-sized or low RCS target is employed.

The reconstructed full-aperture ISAR images are shown in Fig. 11. The outline of the handgun can be discerned from both images, though it is more clearly displayed for the no-covering case. As seen from Fig. 11(b) clothing covering presents a distribution of some cluttering echoes located around the target region, thus masking target signatures. Nevertheless, it is observed that such artifacts do not strongly influence the detection capability, since the current image has strong scattering centers that reflect the shape of the target. However, it may not be always possible to overcome this difficulty, if a small-sized or low RCS target is employed.

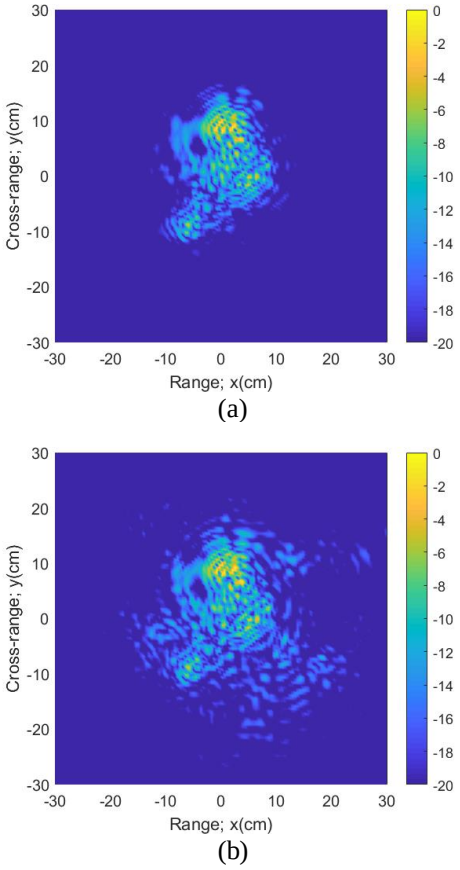

Figure 11. Circular ISAR images for Experiment 5: (a) gun with no covering, (b) gun covered with a jacket.

5. CONCLUSION

In this work, we have presented near-field circular ISAR experiment results that have been conducted in the anechoic chamber at Mersin University's MEATRC facility. Various targets including simple canonic-shaped objects (plates and cylinders) to complex-shaped objects (wrench and hand-gun) have been studied. To compress the ISAR image in angular direction, back-projection type focusing algorithm has been employed. The results from canonical objects have been used to assess the success performance of the imaging study by evaluating the contrast and the resolution metrics of the reconstructed images. Then, realistic targets of a wrench and a handgun were chosen to be objects to be imaged. Reconstructed images have shown the success of the proposed imaging method for imaging small targets (on the order of

centimeters) in near-field ISAR imaging challenge. As the last study, the concealed object detection application has been examined. It has also successfully demonstrated that the ISAR imaging of a handgun can be easily detected and identified even if it is covered with a jacket.

ACKNOWLEDGEMENTS (OPTIONAL)

Authors are grateful to the Mersin University's MEATRC management for their support while conducting the experiments.

REFERENCES

Avşar Aydın, E , Gençoğlan, D. (2016). A bow-tie antenna design for breast cancer detection. The International Journal of Energy and Engineering Sciences, 1 (2), pp. 15-24. Retrieved from https://dergipark.org.tr/tr/pub/ijees/issue/48356/612250

Baird, C., Kersey, W, Giles, R. and Nixon, W. (2005). Exploitation of ISAR imagery in Euler parameter space, Proceedings of SPIE Radar Sensor Technology IX, Vol. 5788, pp. 116–127.

Bertl, S., Dallinger, A. and Detlefsen, J. (2007). Broadband circular interferometric millimetre-wave ISAR for threat detection. Advances in Radio Science, 5, pp. 147-151.

Bertl, S., Dallinger, A. and Detlefsen, J. (2008). Bistatic extension for coherent MMW-ISAR-imaging of objects and humans. Advances in Radio Science, 6, pp. 63-66.

Bertl, S., Dallinger, A. and Detlefsen, J. (2010). Interferometric focusing for the imaging of humans. IET Radar Sonar & Navigation, 4 (3), pp. 457-463.

Bicer, M. B., Akdagli, A. and Ozdemir, C., (2018). A matching-pursuit based approach for detecting and imaging breast cancer tumor. Progress in Electromagnetics Research M, 64, pp. 65-76.

Çelik A. R., Kurt M. B. and Helhel S. (2019). An experimental performance investigation of an ultra-wideband directional antenna in the microwave imaging of breast cancer tumor. Applied Computational Electromagnetics Society Journal, 34, pp.1549-1556.

Cetinkaya, H., Kizilhan. A., Vertiy, A., Demirci, S., Ozdemir, C., Yigit, E., (2011). The millimeter-wave imaging of concealed objects, Spokane-USA, The 2011 IEEE International Symposium on Antennas and Propagation and USNC/URSI National Radio Science Meeting, pp. 228-231.

Chen, C. C. and Andrews, H. C. (1980). Multifrequency imaging of radar turntable data. IEEE Transactions on Aerospace and Electronic Systems, AES-16 (1), pp. 15–22.

Cottard, G. and Arien, Y. (2006). Anechoic chamber measurement improvement. Microwave Journal, 49(3), pp. 94.

Currie, N. C. (1989). Radar reflectivity measurement: Techniques and applications. ISBN: 0890063249, Artech House, Norwood, United States.

Demirci, S., Cetinkaya, H., Tekbas, M., Yigit, E., Ozdemir, C. and Vertiy, A. (2011). Back-projection algorithm for ISAR imaging of near-field concealed objects, Istanbul, Turkey, XXXth URSI 2011 URSI General Assembly and Scientific Symposium.

Demirci, S., Cetinkaya, H., Yigit, E., Ozdemir, C. and Vertiy, A. (2012). A study on millimeter-wave imaging of concealed objects: Application using back-projection algorithm. Progress in Electromagnetics Research (PIER), 128, pp. 457-477.

Demirci, S. and Ozdemir, C. (2013). Compressed sensing based imaging of millimeter-wave ISAR data. Microwave and Optical Technology Letters, 55 (12), pp. 2967-2972.

Demirci, S., Yigit, E. and Ozdemir C. (2015). Wide-field circular SAR imaging: An empirical assessment of layover effects. Microwave Opt. Tech. Letters, 57, (2), pp. 489-497.

Detlefsen, J., Dallinger, A., Huber, S. and Schelkshorn, S. (2005). Effective reconstruction approaches to millimeter-wave imaging of humans, New Delhi, India, Proceedings of the 28th General Assembly of International Union of Radio Science, pp. 23–29.

Hong, C. R. and Büyüköztürk, O. (2000). Wideband microwave imaging of concrete for nondestructive testing. Journal of Structural Engineering, 126 (12), pp. 1451–1457.

Kempf, T., Peichl, M., Dill, S. and Suess, H. (2007). 3D Tower-Turntable ISAR Imaging, Munich, Germany, 2007 European Radar Conference (EuRAD 2007), pp. 114–117.

Knaell, K. and Cardillo, G. P. (1995). Radar tomography for the generation of three-dimensional images. IEE Proceedings - Radar, Sonar and Navigation, 142 (2), pp. 55-60.

Knott, E. F. (2006). Radar cross section measurements. ISBN: 1-891121-55-3, Raleigh, NC, SciTech Publishing.

Mensa, D. L. (1991). High resolution radar cross-section imaging. ISBN: 0890063893, Artech House, Norwood, United States.

Munson, D. C., O'Brien, J. D. and Jenkins, W. K. (1983). A tomographic formulation of spotlight-mode synthetic aperture radar. Proceedings of the IEEE, 71 (8), pp. 917-925.

Naseri, M. (2015). Microwave tomography for breast cancer detection, Thesis (M.Sc.). Istanbul Technical University, Instıtute of Science and Technology.

Ozdemir, C., Kırık, O., Yilmaz, B., (2009). Sub-aperture method for the wide-bandwidth wide-angle inverse synthetic aperture radar imaging, Bursa, Turkey, Int.

Conference on Electrical and Electronics Engineering - ELECO'2009, Bursa, 2, pp. 288-292.

Ozdemir, C. (2012). Inverse synthetic aperture radar imaging with MATLAB algorithms. ISBN: 9780470284841, Wiley Series in Microwave and Optical Engineering, John Wiley & Sons, Inc., Hoboken, New Jersey.

Sheen, D. M., McMakin, D. L. and Hall, T. E. (2010). Near-field three-dimensional radar imaging techniques and applications. Applied Optics, 49 (19), pp. E83-E93.

Soumekh, D. R. (1999). Synthetic aperture radar signal processing with MATLAB Algorithms. ISBN: 0471297062, John Wiley & Sons Inc, New York, United States.

To, L., Bati, A., and Hilliard, D. (2009). Radar cross section measurements of small unmanned air vehicle systems in non-cooperative field environments, Munich, Germany, 2009 3rd European Conference on Antennas and Propagation (EuCAP), pp. 3637–3641.

Wehner, D. R. (1994). High resolution radar. ISBN: 0890067279, Artech House, Norwood, United States.

International Journal of Engineering and Geosciences (IJEG),
Vol; 5, Issue; 3, pp. 160-168, October, 2020, ISSN 2548-0960, Turkey,
DOI: 10.26833/ijeg.650899

ACCURACY ASSESSMENTS OF GÖKTÜRK-1 SATELLITE IMAGERY

Gökhan ARASAN[1], Altan YILMAZ[1*], Orhan FIRAT[1], Ertuğrul AVŞAR[1], Hasan GÜNER[1], Kemal AYĞAN[1], Damla YÜCE[1]
[1]GENERAL DIRECTORATE OF MAPPING, PHOTOGRAMMETRY DEPARTMENT, ANKARA, TURKEY
(GOKHAN.ARASAN@HARITA.GOV.TR ALTAN.YILMAZ@HARITA.GOV.TR; ORHAN.FIRAT@HARITA.GOV.TR; ERTUGRUL.AVSAR@HARITA.GOV.TR; HASAN.GUNER@HARITA.GOV.TR; KEMAL.AYGAN@HARITA.GOV.TR; DAMLA.YUCE@HARITA.GOV.TR); ORCID ID 0000-0002-9163-0950; ORCID ID 0000-0002-1926-0633; ORCID ID 0000-0001-5775-2420; ORCID ID 0000-0003-1397-5870; ORCID ID 0000-0002-9604-9604; ORCID ID 0000-0002-6809-5582; ORCID ID 0000-0002-3343-4775

*Corresponding Author, Received: 25/11/2019, Accepted: 07/03/2020

ABSTRACT: Optical satellite imagery has an important place today in terms of responding to the increasing need for geospatial base in many different fields and disciplines, especially because of their availability and temporal resolution. Because all kinds of geospatial information and data production processes such as orthoimages, maps, vector data and etc. in especially for large project areas provide the opportunity to reduce the cost and time required in the field work, so the interest in high resolution satellite imagery. Göktürk-1, an electro-optical satellite that was launched on December 5, 2016 and acquiring 0.50 m spatial resolution imagery, aims to meet the high resolution image requirements of Turkey.

In this study, the horizontal and vertical accuracy of the Digital Surface Model and orthoimages produced by different methods from stereo images obtained from Göktürk-1 satellite in two different regions were investigated. As a result, although the pointing accuracy and the Digital Surface Model accuracy produced from Göktürk-1 satellite imagery, will vary according to the incidence angle of Göktürk-1 satellite, the Digital Terrain Model used in the production of the orthoimage, the selected method for orientation of satellite imagery; a planimetric accuracy of better than ± 2 m RMSE in orthoimage and a height accuracy of better than ± 3 m RMSE is accomplished.

Keywords: *Göktürk-1, Satellite Imagery, Orthoimage, Orthorectification, Digital Surface Model, Geometric Accuracy*

1. INTRODUCTION

Göktürk-1 satellite was launched from French Guiana on December 5, 2016 with the VEGA system of the European Space Agency. Within the scope of the project, 1 Satellite (0,5 m Electro-Optic), 1 Main Ground Station and 1 Mobile Ground Station were provided.

Göktürk-1 has a flexible view direction. The satellite also has the ability of acquiring 902 spot (15 km x15 km) images and downloading and processing 278 frames (spot) images per day. Direct sensor orientation accuracy of the Göktürk-1 satellite is ± 10 m without using a Ground Control Point (GCP) for images up to 10 ° incidence angle; ± 2 m if sufficient accurate GCPs are provided (Telespazio, 2017, I). The satellite has stereo imaging capability.

The satellite orbits the Earth every 98 minutes, and within 24 hours a total of 14 tours (some days 15). The revisit time of the satellite to display any region of the world is between 2-3 days with an incidence angle of ± 30 °. When the incidence angle is ± 5 °, the revisit time increases to approximately 11 days. The technical characteristics of the satellite are presented in Table 1 (Telespazio, 2017, II).

Table 1. Technical Specifications of Göktürk-1

Specifications	Göktürk-1 Satellite
Orbit Type	Sun Synchronous
Orbit Altitude	681 km
Inclination Angle	98,11°
Period	98 min. 11 sec.
Spot Size	15 km X 15 km
Swath Width	15 km
Strip Length	780 km / 14.300 km
Spatial Resolution	0,5 m PAN – 2 m RGB
Radiometric Resolution	11-Bit
Positional Accuracy	
Horizontal	10 m (without GCP), 2 m (with GCP)
Vertical	20 m (without GCP), 3 m (with GCP)
Spectral Bands	PAN, RGB, NIR
Number of Orbits per Day	14-15 (14,7)
Revisit Time	2-3 days (± 30° incidence) 11 days (± 5° incidence)
Satellite Life	7 years 3 months

Data processing levels and descriptions of GÖKTÜRK-1 satellite images are given in Table 2 (Telespazio, 2017, III).

Table 2. Göktürk-1 Imagery Levels

Image Levels	Definition
Level-0 (L0)	Raw Image
Level-1 (L1)	Radiometric corrected image
Level-2A (L2A)	Geometrically corrected image
Level -2B (L2B)	The image obtained by the L2A image being georectified according to the WGS84 reference system
Level-3A (L3A)	Orthorectified image using Rational Polynomial Coefficients (RPC)
Level -3B (L3B)	Georeferenced and calibrated orthorectified image using GCPs
Level -4 (L4)	Digital Elevation Model (DEM)
Level -5 (L5)	Mosaic image
Level -6 (L6)	Thematic map (Classification)

Rational Function Model Coefficients instead of the physical sensor parameters of the satellite images are provided to the users in order to orient the satellite images. (Tao and Hu, 2002). Since rational functions are proportions of polynomials, they are also called Rational Polynomial Coefficients (RPC). RPCs provided with satellite images can be improved by using different distribution and number of GCPs (Die et al. 2003).

The geometric orientation accuracy of the satellite images using RPC and/or GCP has been assessed in several studies. Cheng and Chaapel (2010) performed 46 cm resolution Worldview-2 satellite geometric accuracy test. They succeeded 2.6 m and 1.3 m accuracies in X and Y directions respectively without using GCPs; obtained 0.7 m and 1.0 m accuracy in X and Y directions respectively using only one GCP. Yilmaz et al. (2016) used aerial photographs and 46 cm resolution Worldview-2 satellites to compare the geometric orientation accuracy. They obtained 1.9, 1.2 m and 2.2 m in X, Y and Z directions respectively without using any GCP. They also obtained one-pixel accuracy in the X and Y directions using a GCP; it at the level of two pixels was in the Z direction.

Because Göktürk-1 has stereo viewing capability, it is possible to produce Digital Elevation Models (DEMs) from stereo or tri-stereo constellations of the imagery. The method for the DEM production from satellite imagery is matching the conjugate points on the overlapped imagery and then apply coplanarity conditions in photogrammetry.

Numerous studies have been conducted to produce DEMs from high resolution satellite imagery. Among the latest ones is the study conducted by Wang et al. (2019). They produced DEM fromWorldview-2 stereo imagery and used for active tectonics. They obtained 1.8 m accuracy without using GCPs and 0.4 m by using GCPs.

Another comprehensive study was held by Perko et al. (2019). In a study by using Pleides satellite stereo imagery, they reached 1.68 m standard deviation in height

in Innsbruck test site by comparing higher accuracy LIDAR data.

In this study, the orthoimagery and the Digital Surface Model (DSM) accuracy produced from stereo Göktürk-1 satellite images in Serik/Antalya region was examined and results were presented.

2. THE SATELLITE IMAGERY AND STUDY AREA

For the horizontal and vertical position accuracy of Göktürk-1 satellite images, two pairs of stereo satellite images covering Serik district of Antalya province and two mono images covering Etimesgut and Yenimahalle districts of Ankara were used. One of the images used in both regions has a low incidence angle (near nadir) and the other is a high incidence angle (far nadir). Also convergence angle was calculated according to Li et al. (2007). Image properties are presented in Table 3.

Table 3. Göktürk-1 Imagery Specifications

Region	Date Time	Incidence	Convergence	Level
Serik (Antalya)	201803310757	7°	32.08°	L2A
	201803310758	30°		L2A
Etimesgut Yenimahalle (Ankara)	201807060752	28°	35.25°	L2A
	201807270753	6.5°		L2A

The study areas are presented in Figure 1.

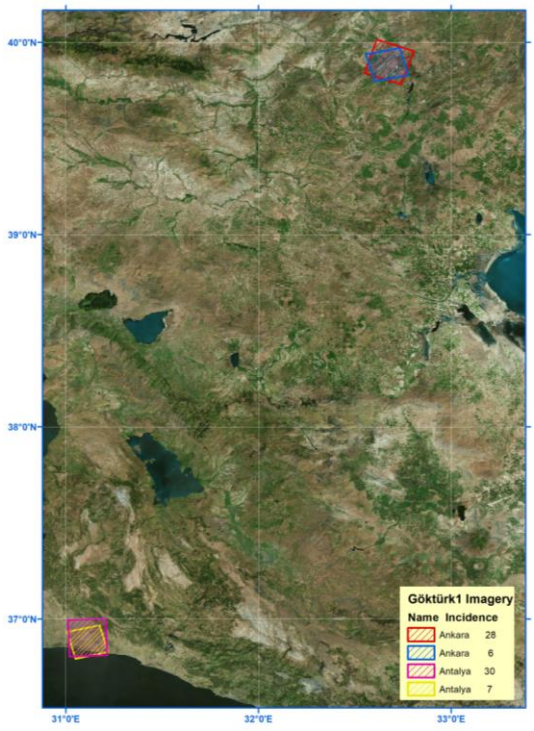

Figure 1. Göktürk-1 Image Pairs in Serik/Antalya and Etimesgut-Yenimahalle/Ankara

Serik test area is located on the south Mediterranean coast of Turkey and also on east side of Antalya city. The area is generally flat. The height ranges between 0 and 210 meters. The sea side is mostly built up with hotels. Serik district center is a medium density built up area. The remaining parts of the test site are agricultural areas. Köprü Stream enters the area from northeast and arrives the sea at southeast. Acısu Stream enters the area from mid-west and arrives the sea at mid-south. The test area has some low hills (~200 meters) in the middle and north parts. The slope in general is between 0° and 5°. The maximum slope on the hilly parts is 30°.

Etimesgut test area is located on the middle of Turkey and also on the west side of Ankara city. The area is generally hilly. The height ranges between 795 and 1305 meters. Etimesgut district center is a high density built up area. The remaining parts of the test site are agricultural areas. There is no stream or lake in the area. The west and south parts are hilly ((~1200 meters). The slope in general (%85) is between 0° and 20°. The maximum slope on the hilly parts is 30°.

GCPs and Check Points (CPs) used in the study for both regions are obtained from 30 cm Ground Sampling Distance (GSD) stereo aerial imagery acquired from Vexcel Ultracam Eagle large format digital aerial cameras with 70% forward and 30% side lap. These control points have a horizontal position accuracy of ± 0.5 m and a vertical position accuracy of ± 0.75 m. The aerial imagery acquisition was performed by General Directorate of Mapping (GDM).

In the orthoimage production, 10 m grid spacing Digital Terrain Model (DTM) produced by GDM was used instead of DTM obtained from stereo satellite images. This is because we want the investigate the accuracy of orthoimages produced from Göktürk-1 satellite imagery by external DTMs. As a result of the comparison of DTM with the CPs in Antalya and Ankara test regions, the vertical RMSEs were ± 3.49 m and ± 4.99 m respectively.

The resulting accuracy of orthoimages rely not only the exterior orientation parameters but also the DEM used in orthoimage production and off-nadir angle of the image. The influence of these error sources on orthoimage accuracy was investigated by Yilmaz and Erdogan (2020). They used an empirical model for defining the errors by using the DEM accuracy and off-nadir angle as variables. They found that vertical RMSE of ± 5 m of the DEM and off-nadir angles between 0° and 20° result ± 0.3 m and ± 1.2 m planimetric errors respectively in the orthoimages.

3. ACCURACY ASSESSMENTS OF GÖKTÜRK-1 SATELLITE IMAGERY

3.1 The Method in the Study

In this study, the orthoimages were produced by 7 different arrangements from near nadir images (low incidence angle) and 3 different arrangements from far nadir (high incidence angle) images in both datasets and the accuracy of these orthoimages was investigated.

DSM was produced by two different methods from both stereo data sets and their accuracy was investigated. Table 4 presents a summary of these methods used in the production of orthoimages and DSM.

The Orthoimages and the DSMs were produced by using PCI GXL and Erdas IMAGINE software.

Table 4. Summary for the arrangements in orthoimage and DSM production

Region	Product	Method					
		Direct Sensor Orientation	1 GCP	5 GCP	10 GCP	15 GCP	20 GCP
Antalya Ankara	Near nadir orthoimage	•	•	•	•	•	•
	Far nadir orthoimage	•	•		•		
Antalya	DSM	•	•				

3.2 Accuracy Assessment in Serik/Antalya Region

Three different methods were used for orthorectification of both near and far nadir Göktürk-1 imagery.

3D geopositioning accuracy of stereo Göktürk-1 pair in Serik was assessed with the same configuration stated in 3.2.1.2 section and the results were presented in Table 5. RMSE and CE90 were obtained from CPs.

Table 5. 3D geopositioning accuracy of Serik Göktürk-1 stereo pair

Number of GCPs	0	1	5	10	15	20
Number of CPs	44	43	39	34	29	24
$RMSE_{xy}$ (± m)	7.67	1.33	1.02	0.84	0.82	0.83
CE90 (± m)	13.18	2.02	1.55	1.27	1.25	1.27
$RMSE_z$ (± m)	1.54	1.08	0.75	0.78	0.76	0.75

3.2.1 Accuracy Assessment in Serik/Antalya Region of Near Nadir Imagery

Two L2A satellite images taken on 31 March 2018 were used in the study. Near nadir image has a 7 ° incidence angle, while a far nadir image has a 30 ° incidence angle. In the study area, 44 points were used as GCP or CPs. The distribution of the GCPs and CPs used in the test with the near nadir image is shown in Figure 2.

Figure 2. Near nadir image and the distribution of GCPs and CPs

3.2.1.1 Orthorectification with Direct Sensor Orientation

In the first method, only the provided RPC parameters was used to orient the satellite imagery and to produce orthoimages as direct sensor orientation. 44 GCPs presented in Figure 2 were used as CPs in order to assess the accuracy.

The statistics of the differences obtained as a result of the comparison between the CPs and orthoimage for the accuracy assessment of the orthoimages are presented in Table 6.

Table 6. Accuracy assessment of the orthoimages produced from Direct Sensor Orientation

Number of GCPs	0
Number of CPs	44
$RMSE_{xy}$ (m)	± 8.48
CE90 (m)	± 12.87

3.2.1.2 Orthorectification by Using GCPs

Göktürk-1 imagery was oriented and orthorectified by using different number of GCPs obtained from stereo aerial imagery. 1, 5, 10, 15 and 20 GCPs were used in orthorectification process. In the first GCP arrangement, only GCP# 131 was used. In the second GCP arrangement, GCP# 103, 119, 123, 131 and 134 were used. In the third GCP arrangement, GCP# 103, 104, 119, 121, 123, 124, 125, 131, 134 and 138 were used. In the fourth GCP arrangement, GCP# 103, 104, 110, 111, 118, 121, 123, 125, 130, 131, 133, 134, 138, 139 and 143 were used. In the fourth GCP arrangement, GCP# 103, 104, 106, 108, 110, 111, 116, 118, 119, 121, 123, 124, 125, 130, 131, 133, 134, 138, 139 and 143 were used. The distribution of GCPs can be traced in Figure 2.

The statistics of the differences obtained as a result of the comparison between the GCPs and orthoimages are presented in Table 7.

Table 7. Accuracy assessment of orthoimages produced by using GCPs

Number of GCPs	1	5	10	15	20
Number of CPs	43	39	34	29	24
$RMSE_{xy}$ (m)	± 1.47	± 1.14	± 1.06	± 1.25	± 0.74
CE90 (m)	± 2.23	± 1.73	± 1.61	± 1.90	± 1.12

3.2.2 Accuracy Assessments in Serik/Antalya Region of Far Nadir Imagery

Orthoimages from the far nadir 30 ° incidence angle at L2A level Göktürk-1 satellite images were produced and analyzed using 1 and 10 GCPs obtained from the stereo models generated from aerial photos of Antalya region in 2015 together with RPC parameters. The distribution of the GCPs or CPs used in the assessment is shown in Figure 3.

Figure 3. Distribution of 51 GCPs and CPs with the far nadir image.

3.2.2.1 Orthorectification with Direct Sensor Orientation

In the first method applied to examine the horizontal positional accuracy of the far nadir image, orthorectification was performed using RPC model determined directly from the orbit parameters and the accuracy of the orthoimage was assessed with 51 CPs shown in Figure 3.

The statistics of the differences obtained as a result of the comparison made at the CPs in order to determine the accuracy of the produced orthoimage are presented in Table 8.

Table 8. Accuracy assessment of orthoimages produced by RPC parameters

Number of GCPs	-
Number of CPs	51
$RMSE_{xy}$ (m)	± 11.14
CE90 (m)	± 16.90

3.2.2.2 Orthorectification with GCPs

The orthoimage is produced by using 1 and 10 GCPs. In the first GCP arrangement, only GCP# 142 was used. In the second GCP arrangement, GCP# 103, 104, 119, 122, 134, 135, 136, 143, 150 and 151 were used. The distribution of GCPs can be traced in Figure 2. The accuracy of the orthoimages is assessed by the CPs that were not used as GCP.

The accuracy assessment of the produced orthoimage by using CPs is presented in Table 9.

Table 9. Accuracy assessment of orthoimages produced by using GCPs

Number of GCPs	1	10
Number of CPs	50	41
$RMSE_{xy}$ (m)	± 2.72	± 2.39
CE90 (m)	± 4.13	± 3.63

As a result of the horizontal accuracy assessment performed in Serik/Antalya region; after orthorectifying the image with an incidence angle of 7° only with RPC parameters, the horizontal positional accuracy was ± 12.87 m in 90% confidence interval, and if the orientation parameters were improved using different quality and number of GCPs, the same accuracy value was changed between ± 1.12 m and 2.23 m.

As a result of orthorectifying an image with an incidence angle of 30 ° only with RPC parameters, the horizontal positional accuracy is ± 16.90 m in the 90% confidence interval, and if the orientation parameters are improved by using 1 and 10 GCPs, the same accuracy value is determined ± 3.63 m to 4.13 m respectively.

Approximately 1.60 m of the decrease in accuracy due to the increase in incidence angle and the DTM used in the production of orthoimages which has an accuracy of approximately 3.50 m in this region.

3.2.3 Accuracy Assessment of DSM

In order to investigate the vertical accuracy, DSM was produced by two different methods. In the first method, DSM was created by using RPC model determined by direct sensor orientation; in the second method, DSM was produced using only 1 GCP. The accuracy of the DEMs produced by both methods was checked with CPs.

3.2.3.1 DSM Production with Direct Sensor Orientation

The accuracy of the DSM produced by direct sensor orientation using only the RPC model was checked by the GCPS presented in Figure 3 as CPs. The statistics on the vertical accuracy statistics of the DSM are presented in Table 10.

Table 10. Accuracy assessment of DSM produced by RPC parameters

Number of GCPs	-
Number of CPs	44
$RMSE_z$ (m)	± 2.84
LE90 (m)	± 4.67

3.2.3.2 DSM Production with GCPs

In the second method, DSM was produced by improving the RPC model by using 1 GCP obtained from the stereo models described in Chapter 2 and presented in

Figure 4. The accuracy of the DSM was checked with the remaining GCPS by using as CPs.

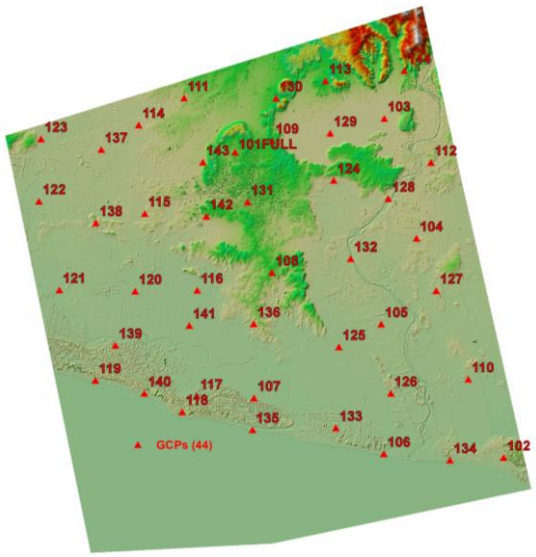

Figure 4. The distribution of CPs

The statistics of the differences obtained as a result of the comparison made at the CPs in order to determine the accuracy of the produced DSM are presented in Table 11.

Table 11. Accuracy assessment of DSM produced by using 1 GCP

Number of GCPs	0	1
Number of CPs	44	43
$RMSE_z$ (m)	± 2.84	± 1.30
LE90 (m)	± 4.67	± 2.14

As a result of the vertical accuracy assessment performed in Serik/Antalya region; it was determined that the accuracy of DSM produced by only RPC parameters from a pair of stereo images was ± 4.67 m in 90% confidence interval and the accuracy of DSM produced by using 1 GCP was ± 2.14 m in 90% confidence interval.

The obtained DSM compared with a superior accuracy reference DSM. This reference DSM is the 5 meters grid spacing DSM produced from 30 cm GSD aerial photos. Detailed information about the reference DSM can be found in Yılmaz and Erdogan (2018). Its' height accuracy is ± 1.3 meter (LE90). Figure 5 shows the difference histogram and accuracy statistics. Even outliers in approximately 50 meters exist, the standard deviation is 1.87 meters.

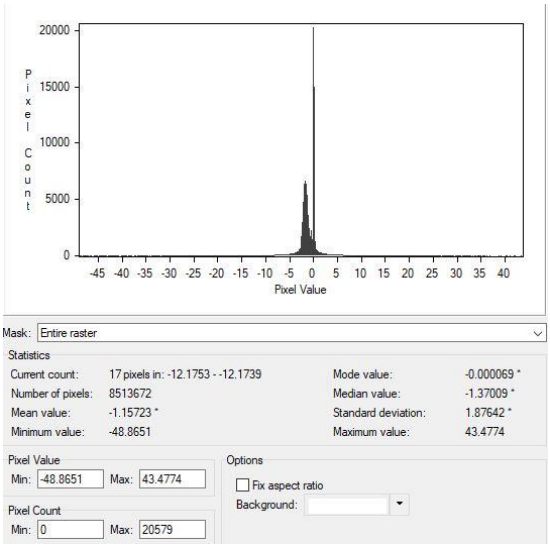

Figure 5. Comparison of Göktürk-1 direct sensor orientation DSM with reference DSM.

3.3 Accuracy Assessment Etimesgut-Yenimahalle/Ankara Region

3.3.1 Accuracy Assessment in Etimesgut-Yenimahalle/Ankara Region of Near Nadir Imagery

L2A level 6.5 ° incidence angle Göktürk-1 satellite image was used to produce orthoimage by using GCPs. 30 GCPs was obtained from the stereo the aerial photos of Ankara region acquired in 2018. The distribution of GCPS is shown in Figure 6.

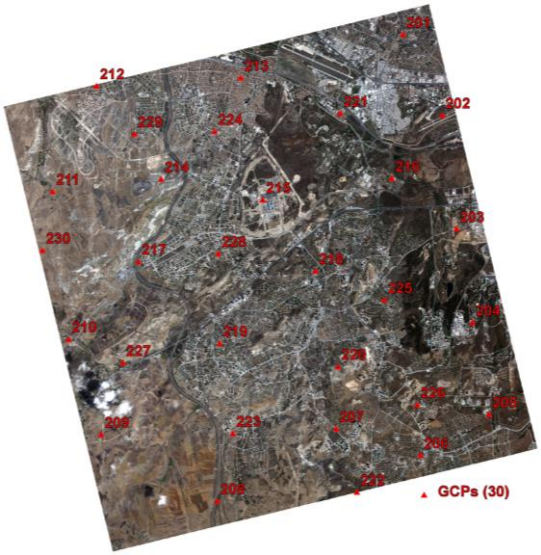

Figure 6. The distribution of 30 GCPs

3.3.1.1 Orthorectification with Direct Sensor Orientation

In the first method to assess the horizontal positional accuracy of the near nadir image, the orthorectification was performed using the RPC model determined directly

from the orbit parameters and the accuracy of the orthoimage was checked with 30 CPs presented in Figure 5.

The statistics of the differences obtained from the comparison at the CPs in order to determine the accuracy of the produced orthoimage are presented in Table 12.

Table 12. Accuracy assessment of the orthoimage produced by using direct sensor orientation

Number of GCPs	-
Number of CPs	30
$RMSE_{xy}$ (m)	± 5.51
CE90 (m)	± 8.36

3.3.1.2 Orthorectification by using GCPs

1,5,10,15 and 20 GCPs obtained from the stereo aerial photos described in Section 2 were used as GCPs and the remaining are as CPs. In the first GCP arrangement, only GCP# 218 was used. In the second GCP arrangement, GCP# 201, 205, 209, 211 and 218 were used. In the third GCP arrangement, GCP# 201, 203, 205, 208, 209, 211, 212, 213, 218 and 222 were used. In the fourth GCP arrangement, GCP# 201, 203, 204, 205, 208, 209, 210, 211, 212, 213, 215, 217, 219, 222 and 225 were used. In the fourth GCP arrangement, GCP# 201, 202, 203, 204, 205, 207, 208, 209, 210, 211, 212, 213, 215, 217, 218, 219, 220, 221, 222 and 225 were used. The distribution of GCPs can be traced in Figure 6. The accuracy of the orthoimages was assessed by the CPs presented in the same figures stated above.

The statistics of the differences obtained from the comparison at the CPs in order to determine the accuracy of the produced orthoimages are presented in Table 13.

Table 13. Accuracy assessment of the orthoimage produced by using different numbers of GCPs

Number of GCPs	1	5	10	15	20
Number of CPs	29	25	20	15	10
$RMSE_{xy}$ (m)	± 0.77	± 0.76	± 0.95	± 0.88	± 0.98
CE90 (m)	± 1.17	± 1.15	± 1.44	± 1.34	± 1.49

3.3.2 Accuracy Assessment in Etimesgut-Yenimahalle/Ankara Region of Far Nadir Imagery

Orthoimages from the far nadir 28 ° incidence angle at L2A level Göktürk-1 satellite images were produced and analyzed using 1 and 10 GCPs obtained from the stereo models generated from aerial photos of Antalya region in 2018 together with RPC parameters. The distribution of the GCPs and CPs used in the assessment is shown in Figure 7.

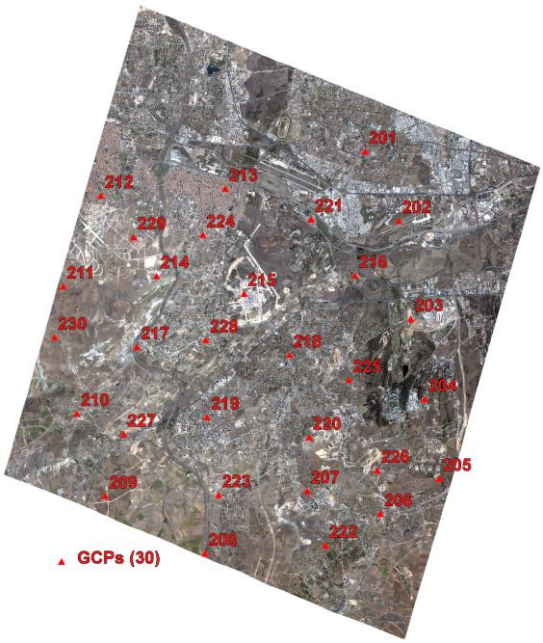

Figure 7. The distribution of 30 GCPs and the far nadir image

3.3.2.1 Orthorectification with Direct Sensor Orientation

In the first method to investigate the horizontal positional accuracy of the far nadir image, orthorectification was performed using the RPC model determined directly from the orbit parameters and the accuracy of the orthoimage was checked with 30 CPs presented in Figure 7.

The statistics of the differences obtained as a result of the comparison of the CPs in order to determine the accuracy of the orthoimage are presented in Table 14.

Table 14. Accuracy assessment of the orthoimage produced by using RPC

Number of GCPs	-
Number of CPs	30
$RMSE_{xy}$ (m)	± 8.35
CE90 (m)	± 12.67

3.3.2.2 Orthorectification by Using GCPs

The orthoimage is produced by using 1 and 10 GCPs. In the first GCP arrangement, only GCP# 218 was used. In the second GCP arrangement, GCP# 201, 203, 206, 208, 210, 212, 213, 217, 218 and 230 were used. The accuracy of the orthoimages is assessed by the CPs that were not used as GCP.

The statistics of the differences obtained as a result of the comparison of the CPs in order to determine the accuracy of the orthoimage are presented in Table 16.

Table 15. Accuracy assessment of orthoimages produced by using GCPs

Number of GCPs	1	10
Number of CPs	29	20
$RMSE_{xy}$ (m)	± 2.75	± 2.11
CE90 (m)	± 4.17	± 3.20

As a result of the horizontal accuracy analysis performed in Etimesgut-Yenimahalle/Ankara region; By the orthorectification of the image with 6.5° incidence angle with only using RPC parameters, the horizontal positional accuracy is ± 8.36 m in 90% confidence interval, and if the orientation parameters are improved using different quality and number of GCPs, the accuracy changes between ± 1.15 m and 1.49 m.

By the orthorectification of the image with 28° angle of incidence with only RPC parameters, the horizontal positional accuracy is ± 16.90 m in 90% confidence interval, and if the orientation parameters are improved by using 1 and 10 GCPs, the accuracy will be ± 3.20 m and 4.17 m respectively.

It is estimated that approximately 2.10 m of the decrease in accuracy due to the increase in incidence angle and also the DTM error, which is used in the production of orthoimages and has an accuracy of approximately 5.00 m in this region.

4. RESULTS AND DISCUSSION

Various arrangements are used in the orthorectification process of the Göktürk-1 satellite images. In this study, the orthoimage and the DSM were produced by using RPC parameters, reference orthoimages and GCPs obtained from the stereo aerial photos. The accuracy of the orthoimages and DSMs were investigated.

The results are summarized in Table 16 and 17.

Table 16. The summary of the accuracy assessment of the orthoimages

Image	Method	ANTALYA				ANKARA			
		Incidence Angle (7°)		Incidence Angle (30°)		Incidence Angle (6.5°)		Incidence Angle (28°)	
		$RMSE_{xy}$ (m)	CE90 (m)	$RMSE_{xy}$ (m)	CE90 (m)	$RMSE_{xy}$ (m)	CE90 (m)	$RMSE_{xy}$ (m)	CE90 (m)
Orthoimage	Direct Sensor Orientaion	±8.48	±12.87	±11.14	±16.90	±5.51	±8.36	±8.35	±12.67
	1 GCP	±1.47	±2.23	±2.72	±4.13	±0.77	±1.17	±2.75	±4.17
	5 GCPs	±1.14	±1.73			±0.76	±1.15		-
	10 GCPs	±1.06	±1.61	±2.39	±3.63	±0.95	±1.44	±2.11	±3.20
	15 GCPs	±1.25	±1.90		-	±0.88	±1.34		-
	20 GCPs	±0.74	±1.12		-	±0.98	±1.49		-

Table 17. The summary of the accuracy assessment of the DSM

IMAGE	Method	ANTALYA	
		$RMSE_z$ (m)	LE90 (m)
DSM	Direct Sensor Orientation	±2.84	±4.67
	1 GCP	±1.30	±2.14

From Göktürk-1 satellite imagery with an incidence angle near nadir (up to 10 °):

• Without using GCP (only with RPC parameters, i.e. direct sensor orientation), in 90% confidence interval, orthoimages better than ± 10 m horizontal accuracy and DSMs better than ± 20 m vertical accuracy can be produced,

• If the orientation parameters are improved by using at least one GCP, it is possible to produce an orthoimage better than ± 2 m horizontal accuracy and DSMs better than ± 3 m vertical accuracy in 90% confidence interval,

• By using only 1 GCP, the accuracy of orthoimage and DSM is improved significantly, and there is no significant improvement in accuracy if more than 1 GCP is used, but it is important to use a large number of evenly distributed GCPs in order to ensure homogeneous accuracy throughout the image,

• Because the convergence angles are very close to each other, the effect of stereo geometry on geopositioning Göktürk-1 imagery cannot be differentiated.

5. CONCLUSIONS

The significant improvement of position by using only one GCP shows that a shift effect exists in both planimetry and vertical positioning of the satellite's RPC. Although using more than one GCP does not reflect meaningful improvement in geopositioning, it is always safe using more than one GCP. Because using one GCP susceptible to the random geopositioning errors of that GCP.

Further studies on Göktürk-1 imagery can be carried out especially about tri-stereo geopositioning accuracies and off-nadir accuracy change on the imagery that can be modelled.

ACKNOWLEDGEMENT

The subjects written here do not represent the ideas of Turkish Armed Forces.

REFERENCES

Cheng P. and Chaapel C., 2010. Pan-sharpening and geometric correction of WorldView-2 satellite. GEOInformatics 2010:30–33

Di, K., Ma R. and Li R., 2003. Rational functions and potential for rigorous sensor model recovery. Photogrammetric Engineering and Remote Sensing, 69(1), 33-41

Li, R., Zhou F., Niu X., and Di K., 2007. Integration of Ikonos and QuickBird Imagery for geopositioning accuracy analysis. Photogrammetric Engineering & Remote Sensing, 73 (9):1067–1074.

Perko, R., Raggam, H. and Roth, P.M., 2019. Mapping with Pléiades—End-to-End Workflow. Remote Sensing 11 (17) 2052. DOI 10.3390/rs11172052

Tao, V. and Hu, Y. 2002. 3D Reconstruction methods based on the rational function model. Photogrammetric Engineering Remote Sensing 68(7):705–714

Telespazio, 2017 I. Göktürk-1 User Guide

Telespazio, 2017 II. Göktürk-1 System Specification Technical Notes

Telespazio, 2017 III. Göktürk-1 Product Specification Definitions Technical Notes

Wang, S., Ren, Z., Wu, C., Lei, Q., Gong, W., Ou, Q., Zhang, H., Ren, G. and Li, C., 2019. DEM generation from Worldview-2 stereo imagery and vertical accuracy assessment for its application in active tectonics. Geomorphology. 336:107-118. DOI 10.1016/j.geomorph.2019.03.016.

Yilmaz A., Erdogan M., Maras H.H., Aktug B. and Maras S.S., 2016. Did satellite imagery supersede aerial imagery? A perspective from 3D geopositioning accuracy. Arabian Journal of Geosciences (2016) 9: 324 DOI 10.1007/s12517-016-2386-x.

Yilmaz A. and Erdogan M., 2020. Modelling the orthoimage accuracy using DEM accuracy and off-nadir angle, Geocarto International, 35 (1), 1-16. DOI: 10.1080/10106049.2018.1493157.

Yilmaz A. and Erdogan M., 2018. Designing High Resolution Countrywide DEM For Turkey. International Journal of Engineering and Geosciences, 3 (3), 98-107. DOI: 10.26833/ijeg.384822.

International Journal of Engineering and Geosciences

IJEG
Volume 5 - Issue 3

ARTICLES